HHS Public Access

Author manuscript

Mol Cell. Author manuscript; available in PMC 2021 November 05.

Published in final edited form as:

Mol Cell. 2020 November 05; 80(3): 525–540.e9. doi:10.1016/j.molcel.2020.09.022.

Characterization of metabolic patterns in mouse oocytes during meiotic maturation

Ling Li[1,8], **Shuai Zhu**[1,8], **Wenjie Shu**[2,8], **Yueshuai Guo**[1,8], **Yusheng Guan**[1,3], **Juan Zeng**[1], **Haichao Wang**[1], **Longsen Han**[1], **Jiaqi Zhang**[1], **Xiaohui Liu**[4], **Chunling Li**[1], **Xiaojing Hou**[1], **Min Gao**[4], **Juan Ge**[1], **Chao Ren**[2], **Hao Zhang**[1,6], **Tim Schedl**[5], **Xuejiang Guo**[1,6,*], **Minjian Chen**[1,3,*], **Qiang Wang**[1,7,9,*]

[1]State Key Laboratory of Reproductive Medicine, Suzhou Municipal Hospital, Nanjing Medical University, Nanjing 211166, China

[2]Department of Biotechnology, Beijing Institute of Radiation Medicine, Beijing 100850, China

[3]Key Laboratory of Modern Toxicology of Ministry of Education, School of Public Health, Nanjing Medical University, Nanjing 211166, China

[4]College of Animal Science and Technology, Nanjing Agricultural University, Nanjing 210095, China

[5]Department of Genetics, Washington University School of Medicine, St Louis, Missouri 63110, USA

[6]Department of Histology and Embryology, Nanjing Medical University, Nanjing 211166, China

[7]Center for Global Health, School of Public Health, Nanjing Medical University, Nanjing 211166, China

[8]These authors contributed equally

[9]Lead contact

SUMMARY

Well balanced and timed metabolism is essential for making a high quality egg. However, the metabolic framework that supports oocyte development remains poorly understood. Here we obtained the temporal metabolome profiles of mouse oocytes during *in vivo* maturation by isolating large number of cells at key stages. In parallel, quantitative proteomic analyses were

*Correspondence: qwang2012@njmu.edu.cn (Q.W.), guo_xuejiang@njmu.edu.cn (X.G.), minjianchen@njmu.edu.cn (M.C.).

AUTHOR CONTRIBUTION

Q.W., M.C. and T.S. conceived the projects. M.C. and Y.G. contributed to the metabolomics profiling; Y.G., H.Z. and X.G. contributed to the proteomic profiling. L.L., S.Z., J.Z., H.W. and M.G. performed the mechanistic experiments. W.S. and C.R. contributed to the DNA methylome analysis. L.H., J.Z., X.H., X.L., C.L. and J.G. performed the oocyte/embryo collection and culture experiments. Q.W. wrote, and T.S. revised the manuscript.

DECLARATION OF INTERESTS

The authors declare no competing interests.

conducted to bolster the metabolomic data, synergistically depicting the global metabolic patterns in oocytes. In particular, we discovered the metabolic features during meiotic maturation, such as the fall in polyunsaturated fatty acids (PUFAs) level and the active serine-glycine-one-carbon (SGOC) pathway. Using functional approaches, we further identified the key targets mediating the action of PUFA arachidonic acid (ARA) on meiotic maturation, and demonstrated the control of epigenetic marks in maturing oocytes by SGOC network. Our data serves as a broad resource on the dynamics occurring in metabolome and proteome during oocyte maturation.

Graphical Abstract

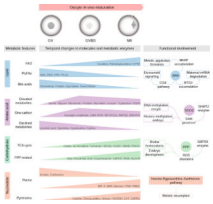

INTRODUCTION

Reproduction is tightly connected with metabolic state of the organism. Oocyte development is particularly sensitive to the alterations in nutritional and chemical environments (Hunt and Hassold, 2008). Moreover, emerging evidence indicates that impaired oocyte quality represents a critical mechanism mediating the inter/transgenerational phenotypes induced by maternal metabolic syndrome, such as obesity, diabetes, and polycystic ovary syndrome (PCOS) (Han et al., 2018; Huypens et al., 2016; Risal et al., 2019). Well balanced and timed metabolism is essential for producing developmentally competent eggs (Gu et al., 2015). Despite these links, the metabolic framework that supports oocyte growth and maturation is still not fully understood.

Oocytes originate from primordial germ cells (PGCs), which then undergo mitosis, transforming from oogonia into primordial oocytes. Around the time of birth, oocytes are arrested in prophase I of meiosis, which is also called the germinal vesicle (GV) stage. Oocyte growth culminates just prior to ovulation, when oocyte maturation occurs. Upon hormonal surge, immature oocytes resume meiosis, characterized by GV breakdown (GVBD). Accompanying with the chromatin condensation and microtubule organization, the oocytes proceed through the meiosis I (MI) division, and then become arrested again at metaphase II (MII), awaiting for fertilization (Wang and Sun, 2007). The basic pattern of metabolism in mammalian oocytes was established in the 1960s, largely in terms of the consumption of oxygen and the utilization of nutrients present in culture media (Leese, 2015). A series of fundamental findings in this field have been successively discovered, mainly by using radioisotopically labeled substrates. For instance, the fully grown oocytes have a limited capacity to metabolize glucose through glycolysis (Biggers et al., 1967; Leese and Barton, 1985; Saito et al., 1994), and follicular cells provide sufficient pyruvate to ensure successful meiotic maturation (Downs and Mastropolo, 1994; Eppig, 1976; Fagbohun and Downs, 1992). Lipid droplets are stored in the cytoplasm during mammalian oogenesis, although their content varies widely among species (Ferguson and Leese, 1999; Homa et al.,

1986; Loewenstein and Cohen, 1964; McEvoy et al., 2000). A growing number of reports have shown that inhibition of fatty acid oxidation disrupts oocyte meiotic resumption and developmental potential (Downs et al., 2009; Dunning et al., 2010; Ferguson and Leese, 2006). On the other hand, intrinsic control of oogenesis by intracellular metabolites and metabolic enzymes has received little attention. While the existing studies identified several cellular pathways, we believed that a global search of metabolic patterns could lead to more complete understanding of oocyte development.

In the present study, we obtained dynamic metabolome profile of mouse oocytes during *in vivo* maturation by isolating large number of cells at key stages. Furthermore, we bolstered the metabolomics studies with quantitative proteomic analyses. Meanwhile, we experimentally manipulated specific pathways in oocytes, and uncovered the molecular mechanisms controlling meiotic maturation through fatty acid and amino acid metabolism. Our data serves as a broad resource for probing mammalian oocyte metabolism, provides opportunities for the discovery of biomarkers in the prediction and improvement of oocyte quality and female fertility.

RESULTS

Metabolomic and proteomic profiling of mouse oocyte maturation

Although changes in *in vitro* oocyte metabolism have been reported, a comprehensive investigation of metabolite dynamics during *in vivo* oocyte maturation is lacking. This is in large part due to limited amounts of experimental material. The oocyte is the largest cell in the mammalian female, but available in very small numbers compared to somatic cells (Leese, 2015). Here, we isolated large numbers of mouse oocytes (totally 54,000 oocytes) at three key time points during meiotic maturation (arrested GV stage, meiotic resumption GVBD stage, and ovulated MII oocyte), and analyzed the intracellular metabolome using ultra-high-performance liquid chromatography-tandem high-resolution mass spectrometry (UHPLC-HRMS) (Figures 1A-1B). A total of 57 differential metabolites were identified, based on a T-test ($P < 0.05$) coupled with a variable importance in projection (VIP) analysis (VIP > 1.00) (Table S1). Robust orthogonal partial least squares-discriminant analysis (OPLS-DA) clearly showed stage-dependent separation of the three oocyte groups with the cross validated predictive ability of Q2 (cum) ≥ 0.832 (Figures 1C-1E). Changes in metabolite level during meiotic maturation are represented as a heat map (Figure 1F). The differential metabolomics profiles where mapped to their respective biochemical pathways, delineated in Kyoto Encyclopedia of Genes and Genomes (KEGG), revealing distinct metabolite patterns (Figure 1F). In general, amino acids/carbohydrates/nucleotides increased during meiotic resumption, GV to GVBD, or meiotic maturation, GV to MII, whereas lipid metabolites displayed a notable reduction during meiotic resumption (Figures 1F-1H).

Metabolic enzymes are the mediators of cellular metabolism. To determine whether changes in substrates/products were correlated with a corresponding change in enzymatic protein accumulation, we simultaneously conducted a quantitative proteomic analysis of GV, GVBD and MII oocytes (Figure S1A). 46,016 peptides were detected, 4,694 proteins were quantified, and a total of 2,081 proteins with differential levels were identified (false discovery rate [FDR] = 0.05) (Figure S1B; Table S2). Gene ontology (GO) analysis showed

a significant enrichment of categories related to metabolic pathways such as glutathione/carbon/pyruvate metabolism and TriCarboxylicAcid cycle (TCA cycle) (Figures S1C-S1D). To better understand the metabolic involvement in oocyte development, we also mapped all enzymes with differential accumulation to the main KEGG metabolic pathways, revealing numerous markedly altered events/processes during meiotic maturation (i.e. oxidative phosphorylation and cofactor/vitamin metabolism) (Figure S2). Together, these data provide a broad resource of metabolome and proteome dynamics during *in vivo* mouse oocyte maturation. Below we use the metabolomic and proteomic data as an entree to elaborate on possible consequences of the metabolite changes for oocyte maturation and the transition to zygotic development and to uncover the mechanisms that are necessary for mammalian meiotic maturation.

Lipid metabolism during oocyte maturation

From the metabolite map of oocytes (Figure 1F), we observed two distinct patterns of lipid metabolism during oocyte maturation. Levels of carnitine and palmitoylcarnitine in meiotic resumption were dramatically elevated compared to immature GV oocytes (Figures 2A-2B). In contrast, the majority of detected lipid metabolism-related products (i.e. arachidonic acid, docosahexaenoic acid, eicosapentaenoic acid, cholesterol, cholic acid, glycocholic acid, taurocholic acid, octadecanamide, and dodecanoic acid) declined as the oocytes progress through meiosis (Figures 2C-2H; Figure S3). These observations indicate the differing roles of lipid metabolism in meiotic oocytes, as reported below.

Maturation stage-dependent increase in fatty acid utilization in oocytes: The major pathway for the degradation of long-chain fatty acid is mitochondrial fatty acid beta–oxidation (FAO). Fatty acyl-CoAs are generated on the outer mitochondrial membrane and converted to the fatty acylcarnitines (i.e. palmitoylcarnitine) by carnitine palmitoyltransferase I (CPTI). Acylcarnitine passes through a carnitine-acylcarnitine translocase to the inner part of the inner mitochondrial membrane, where carnitine palmitoyltransferase II (CPTII) converts fatty acylcarnitines into fatty acyl-CoAs, that can undergo beta–oxidation in the mitochondrial matrix (Goni et al., 1996) (Figure 2I). Although FAO has been implicated to be important for maturation of mouse oocytes (Downs et al., 2009; Dunning et al., 2010), the metabolic basis underlying this process remains unclear. Of note, our metabolomic analysis identified a 3–4-fold increase in carnitine and palmitoylcarnitine content in oocytes, during meiotic resumption (Figures 2A-2B). Meanwhile, the proteomic data showed reproducible and statistically significant upregulation of CPTII level (Figure 2I), suggesting enhancement of FAO activity. Moreover, an integrated analysis of proteomic temporal profiles and metabolic pathways revealed that 7 out of 8 enzymes detected involved in fatty acid degradation (ACOX3, ACAT1, ECHS1, HADHA, ALDH2, ALDH3A2, and ALDH7A1) were elevated in ovulated MII oocytes compared to GV oocytes (Figure S4). These data strongly suggest enhanced utilization of fatty acid during mouse oocyte maturation.

Reduction in bile acids and their derivatives during oocyte maturation: Bile acids are amphipathic molecules synthesized from cholesterol. They have largely been considered as biological detergents that dissolve lipids and lipid-soluble vitamins (de Aguiar

Vallim et al., 2013), although recent literature describes bile acids as versatile signaling molecules (Mertens et al., 2017). To date, however, the levels of cholesterol and bile acids during oocyte maturation are unknown. We found that cholesterol levels decrease in the transition from GV to MII arrested oocytes (Figure S3A). Similarly, the levels of cholic acid and its derivatives (glycocholic acid and taurocholic acid) significantly decrease upon meiotic resumption (Figures 2C-2E). Previous work showed that excess cholesterol, *in vivo* and *in vitro*, led to spontaneous activation and escape from MII arrest, in the absence of fertilization (Yesilaltay et al., 2014). Therefore, the fall we observe in cholesterol, and possibly bile acids, is likely a reflection of the need to decrease cholesterol levels to promote the MII arrest.

Involvement of PUFAs metabolism in oocyte maturation: Mammals can elongate and desaturate linoleic acid to produce a range of long chain polyunsaturated fatty acids (PUFAs). We found that levels of PUFAs arachidonic acid (ARA), docosahexaenoic acid (DHA) and eicosapentaenoic acid (EPA) fall during meiotic resumption (Figures 2F-2H; Table S1). Eicosanoids are synthesized from ARA in response to a stimulus, which induces cytoplasmic phospholipase A2 (PLA2) to translocate to endoplasmic reticulum, Golgi apparatus, or nuclear membrane where it catalyzes the release of a PUFA from a phospholipid membrane. Free PUFAs can be processed either by cyclooxygenase enzymes (COX1/2) to form prostaglandins/thromboxanes or by lipoxygenase (LOX) to form leukotrienes family of eicosanoids (Vrablik and Watts, 2013) (Figure S5A). While PUFAs and their signaling derivatives (eicosanoids) participate in variety of biological processes, little is known about how these metabolites exert their effects on mammalian oocytes. First, we examined the potential involvement of different PUFA metabolic pathways in oocyte maturation using small-molecule inhibitors. As shown in Figures S5B-S5C, inhibition of Δ6/Δ5-desaturase with sesamin or curcumin appeared to affect neither the GVBD nor the polar body (Pb1) emission, suggesting that PUFAs synthesis from linoleic acid is likely dispensable for oocyte maturation or that there may be sufficient ARA/DHA/EPA at the GV stage for normal meiotic maturation. Of note, proteomic data showed the gradual reduction in PLA2 level during maturation (Figure S5A). Considering the lowered levels of PUFAs in ovulated oocytes, we propose that PLA2-controlled release from phospholipid molecules is a major source of ARA/DHA/EPA in mouse oocytes. Significantly, we found that inhibition of COX with INDO, and to a lesser extent inhibition of LOX with BWA4C, resulted in a dosage-dependent decrease in meiotic maturation rate (Figures S5B-S5C). This suggests that the oocytes synthesize prostaglandins/leukotrienes via PUFAs catabolism for a possible autocrine function to promote meiotic maturation.

To test whether the decrease in intracellular PUFAs was important for meiotic maturation, we asked if elevating PUFA availability disrupts oocyte maturation. In brief, fully grown GV oocytes were cultured in medium supplemented with various concentrations of ARA, and then relevant maturation phenotypes were examined at the indicated time points (Figure 2J). ARA treatment had little effect on oocyte GVBD (data not shown); however, the Pb1 extrusion was reduced in a dose-dependent manner (Figures 2K-2L), indicating a disruption of the meiosis I division. Washout experiments showed that the ARA inhibitory effect was almost completely reversible (Figure 2M). Moreover, we found that ARA supplementation

resulted in a high frequency of meiotic defects in metaphase I oocytes including spindle disorganization and chromosome misalignment (Figures 2N-2O). In some cells, the spindle was not even formed, with the presence of irregular chromatin lump (Figure 2N; arrows), reflecting the alterations in meiotic structure. We determined that intracellular ARA level was increased 1.5- to 2.0-fold at 7 hours in oocytes cultured in ARA-supplemented medium, compared to controls (Figure 2P), a change in ARA level consistent with the fall during meiotic resumption detected *in vivo*. Similar effects of DHA/EPA administration on oocyte maturation were also observed (Figure S6; Figure S7). The observation that the level of ARA/PUFAs fall during meiotic resumption and the finding that excess ARA/PUFAs disrupt meiotic maturation leads to the hypothesis that ARA/PUFA signaling suppresses oocyte maturation and must be downregulated to relieve this inhibitory mechanism.

Identification of targets of ARA inhibition that promote meiotic maturation

To elucidate potential mechanisms by which the decrease in ARA levels promotes oocyte maturation, we performed a comparative proteomic analysis of oocytes cultured for 7 hours in medium with or without ARA (Figure 3A). A total of 35,344 peptides were detected, and the accumulation of 87 out of 3787 proteins was significantly altered in ARA-treated oocytes (FDR = 0.05, Log2 fc >1.5; Figures 3B-3C; Table S3). GO analysis indicated that many of the proteins with differential accumulation were enriched in meiosis, cell cycle and RNA processing (Figure. 3D). Of them, NFKB activating protein (NKAP) and B cell translocation gene 4 (BTG4) are of great interest because; (*i*) NKAP is a highly conserved protein with roles in mitosis and transcriptional modulation (Burgute et al., 2014; Li et al., 2016). Significantly, similar to what we observed in ARA-treated oocytes, loss of NKAP causes chromosome misalignment, pre-metaphase arrest, and aneuploidy in human cells (Li et al., 2016). (*ii*) As an essential factor modulating maternal mRNA stability, BTG4 expression experienced a dramatic increase during normal oocyte maturation (Table S2; GVBD/GV: ~3-fold and MII/GV: ~99-fold).

ARA modulates the meiotic apparatus in oocytes by controlling NKAP accumulation: We first validated the proteomic data, showing by Western blot analysis that there was a ~70% reduction of NKAP level in ARA-treated oocytes (Figure 3E). Immunostaining revealed that NKAP resides in the cytoplasm and nucleus of GV oocytes. Once the oocytes have resumed meiosis, NKAP becomes concentrated on the spindle region (Figure 3F), indicating that it may have a function in the formation or stability of meiotic apparatus. To test this probability, fully grown oocytes were microinjected with *Nkap*-targeting siRNA (siNkap) (Figure S8A), leading to a significant reduction in NKAP protein (Figure S8B). Although siNkap oocytes underwent GVBD normally, Pb1 extrusion was significantly reduced compared to controls (Figures S8B-S8E), indicative of a maturation defect. In particular, spindle disorganization and chromosome congression failure were readily detected in oocytes depleted of NKAP (Figures S8F-S8G), similar to the phenotypes of ARA-treated oocytes. Coordination between spindle maintenance and chromosome movement relies on kinetochore microtubule dynamics (Nezi and Musacchio, 2009). In line with this notion, NKAP knockdown induces high frequency of the kinetochore-microtubule (K-MT) mis-attachments in MI stage oocytes (Figures S8H-S8I), resulting in unstable chromosome biorientation. The mechanism that monitors and responds to K-MT attachment

is the spindle assembly checkpoint (Nezi and Musacchio) (Brunet et al., 2003; Nezi and Musacchio). BubR1 is an integral part of SAC complex. In normal metaphase oocytes, BubR1 is lost from kinetochores when properly attached to chromosomes. However, BubR1 signal on the kinetochores was markedly increased in siNkap oocytes (Figures S8J-S8K), indicating that SAC activation contributes to the maturation defect. The specificity of siNkap knockdown was confirmed by an mRNA rescue experiment (Figures S13A-S13D). These data identify NKAP as an important player in modulating meiotic structure and maturational progression in oocytes. Given the reduction of NKAP accumulation in ARA-treated oocytes, we tested whether elevating NKAP level could suppress one or more of oocyte maturation defects. Toward this goal, we performed overexpression experiments by injecting *Nkap*-cRNA into GV oocytes treated with ARA (Figure 3G). Western blotting confirmed that exogenous NKAP protein was efficiently expressed in oocytes (Figure 3H). Importantly, the spindle and maturation defects induced by ARA supplementation were partially suppressed by overexpression of NKAP (Figures 3I-3K). Collectively, these results indicate that NKAP has an important role in the assembly of meiotic apparatus, and that this activity is suppressed by high levels of ARA at the GV stage, but relieved as ARA levels fall during meiotic resumption.

ARA influences BTG4-controlled mRNA degradation during meiotic maturation: Meiotic resumption-coupled degradation of oocytes transcripts occurs in the absence of mRNA transcription (Sha et al., 2019). BTG4 has been shown to trigger decay of oocyte mRNA by stimulating the deadenylation of their poly(A) tails during meiotic maturation (Pasternak et al., 2016; Yu et al., 2016). Similar to proteomic data, Western blotting demonstrated that BTG4 level was decreased by ~80% in ARA-treated oocytes relative to controls (Figure 3L). We then asked whether mRNA stability in oocytes was disturbed due to ARA supplementation during maturation. To address this question, we evaluated polyadenylation levels of several representative maternal transcripts (*Padi6*, *Nobox*, *ZP2* and *Fgf8*) in oocytes using poly(A) tail (PAT) assay (Figure 3M). Consistent with previous report (Yu et al., 2016), poly(A) tails were shortened in control maturing oocytes; but remarkably, this process was blocked in ARA-treated oocytes (Figures 3N-3R), and the corresponding transcripts were thus resistant to degradation (Figure 3S). These data indicate that the fall in ARA during meiotic resumption allows BTG4 to accumulate, triggering the degradation of maternal RNAs.

Differential patterns of amino acid metabolism during oocyte maturation

In addition to changes in fatty acid metabolism, our temporal metabolite profiles showed alterations in level of certain amino acid during oocyte maturation (Figure 4; Figure S9). The abundance of most amino acids we detected (i.e. serine, glutamate and histidine) significantly increased during meiotic resumption, and then reduced in matured oocytes (Figures 4A-4H; Table S1 with GVBD>MII stats). In contrast, some amino acids (i.e. glycine and norvaline) continually increased from GV to MII stage (Figures 4I-4J). The levels of other amino acids (i.e. levulinic acid, cystine and hypotaurine) decreased during meiotic resumption (Figures. S9E-S9H). The reduction in level of standard amino acids can, at least in part, be attributed to utilization in ongoing translation of constitutively translated mRNAs and the recruitment of new mRNA species to polysomes during oocyte maturation

(Chen et al., 2011). Amino acids are also intermediates in nucleotide and lipid synthesis, carbon and nitrogen homeostasis, and redox buffering. Therefore, such a diversity of metabolic trends in oocytes reflects the complicated and fine-tuned regulation of amino acid metabolism.

Upregulated Serine-Glycine-One-Carbon pathway during meiotic resumption: We found that numerous metabolites in the methionine cycle (i.e. S-adenosylmethionine [SAM] and 5'-methylthioadenosine [MTA]) and the transsulfuration pathway (i.e. glutamate and pyroglutamic acid) were elevated during meiotic resumption (Figure 4K). Proteomic profiles showed increased levels of enzymes related to the folate cycle, the methionine cycle, and the transsulfuration pathway in matured oocytes (Figures 4L-4N; Figures S9I-S9M). The transsulfuration pathway entails the transfer of the sulfur atom of methionine to serine to yield cysteine, which could be utilized for glutathione (GSH) synthesis, defending against oxidative stress. The Serine-Glycine-One-Carbon (SGOC) pathway is a metabolic network that consists of two core interconnected cycles: the folate and the methionine cycles. The outputs of SGOC pathway include key metabolites that maintain the biosynthesis of nucleotides, proteins, and lipids; it also fuels methyltransferase reactions that shape the epigenetic landscape (Reina-Campos et al., 2020). Taking into account the robust increase in serine/glycine level (up to 10–12-fold), the findings above strongly indicate that the SGOC pathway is upregulated during meiotic resumption.

SHMT2 depletion impairs the epigenetic landscape in matured oocytes: Serine feeds into the central core of the SGOC pathway via the enzyme serine hydroxymethyl transferases (SHMT1/2), which converts serine (three carbons) into glycine (two carbons), transferring one carbon to tetrahydrofolate (THF) (Figure 4K). Mice lacking SHMT1 have no overt phenotype, whereas loss of SHMT2 is embryonic lethal, suggesting that the mitochondrial SHMT2 may be more important and thus compensate for the loss of cytoplasmic SHMT1 (MacFarlane et al., 2008; Momb et al., 2013; Tani et al., 2018). To examine the functional involvement of SGOC metabolism in oocyte development, we carried out SHMT2 knockdown experiments (Figure 5A). Endogenous SHMT2 protein was efficiently depleted by siRNA injection (Figure 5B). We found that the serine/glycine ratio was increased in the knockdown, relative to the control, consistent with glycine being the product of the SHMT2 reaction (Figure 5C). Notably, SAM levels were significantly lowered (Figure 5D), consistent with diminished SGOC pathway activity in siShmt2 oocytes. As shown in Figure 5E, SHMT2 loss appeared not to have a significant effect on execution of meiotic maturation, albeit a slight decrease in Pb1 extrusion was detected. Importantly, after fertilization, only ~30% of embryos derived from Shmt2 knockdown oocytes developed to 2-cell stage on day 1.5, which is significantly lower than controls (Figures 5F-5G), reflecting the compromised developmental potential of oocytes. siShmt2 specificity was confirmed by performing an mRNA rescue experiment (Figures S13E-S13G).

All methytransferase reactions in mammalian cells rely exclusively on the methyl donor SAM, an important SGOC output (Maddocks et al., 2016). Considering dynamics of SAM

levels in normal oocyte maturation, elevated in GVBD oocytes, then reduced at MII, we next sought to assess the effects of SHMT2 knockdown on the oocyte epigenomic landscape. Control and siShmt2 MII oocytes were collected for genome-wide DNA methylation profiling using the bisulfite sequencing (BS-seq) method for small samples (Figure 5H), as we described previously (Han et al., 2018). The data demonstrated a reduction in mean genome methylation (Figures 5I-5J). Comparative analysis of distinct genomic features further revealed significant hypomethylation in the repetitive elements (Figures 5K-5M; Figures S10A-S10K), particular low copy repeats (LCRs), transposons, and short interspersed nuclear elements (SINEs). Moreover, we found that the differentially-methylated LCRs are significantly depleted from intergenic regions, but enriched in 5' untranslated region (UTR), exons, and promoters (Figure S10L). Next, we asked whether the reduced SAM levels in oocytes would thereby impact the epigenetic modifications of the resultant embryos. To do this, we conducted *in vitro* fertilization (IVF) of control and siShmt2 oocytes, and then zygotes were collected to check the state of histone methylation (H3K4me3/H3K9me2/H3K27me3). Of them, H3K4me3 levels were significantly reduced in the maternal pronucleus (PN) upon SHMT2 depletion (Figures 5N-5O). Both CpG and non-CpG *de novo* DNA methylation increase during meiotic maturation (Smallwood et al., 2011; Yu et al., 2017). We hypothesize that SHMT2 activity is required for SAM generation during meiotic resumption, with the fall in SAM level by MII, at least in part, a consequence of its utilization in DNA methylation. These results indicate that SGOC mediated SAM production during meiotic maturation is important to establish the appropriate epigenetic marks for the oocyte to embryo transition.

Carbohydrate metabolism during oocyte maturation

It has been widely accepted that carbohydrate metabolism is essential for oogenesis (Harris et al., 2007). However, data showing carbohydrate dynamics during oocyte maturation is lacking. Temporal metabolome profiles clearly revealed a number of carbohydrate metabolites increased during oocyte maturation (Figures 6A-6H), with enrichment primarily in the TCA cycle and pentose phosphate pathway (PPP).

Enhanced TCA cycle activity and pyruvate oxidation during maturation: The abundance of three key components of TCA cycle underwent a dramatic increase (citrate: ~5-fold; cis-Aconitate: ~6-fold; fumarate: ~2-fold) in maturing oocytes (Figures 6A-6C and 6J). Furthermore, out of 10 TCA cycle enzymes we detected, 8 experienced consistent and statistically significant upregulation during meiotic maturation (Figures 6K-6O; Figure S11), suggesting activation of TCA cycle. In addition, accumulation of three enzymes of pyruvate dehydrogenase (PDH) complex including PDHA1, dihydrolipoyl transacetylase (DLAT), and dihydrolipoyl dehydrogenase (DLD), were all elevated during maturation (Figure 6J; Figure S11). PDH complex is responsible for the oxidative decarboxylation of pyruvate, with the final product being acetyl CoA, and thereupon modulates the entry of glucose-derived carbons into TCA cycle. Integrated analysis of metabolomic and proteomic data (Figure S11) highlights the coordinated upregulation of metabolite level and enzyme accumulation. Altogether, the results indicate that generation of a competent egg requires the enhanced pyruvate metabolism and TCA cycle activity.

Active PPP functions in meiotic oocytes: Substantial evidence indicates that oocytes have low glycolytic activity (Sutton-McDowall et al., 2010). Consistent with this notion, very few metabolites and enzymes involved in glycolysis were found to change during meiotic maturation based on our metabolomic and proteomic analysis. In contrast, several key intermediates of the PPP exhibited dramatic changes. For instance, a ~30-fold-increase in glucose-6-phophate and gluconolactone and a ~10-fold-increase in glucuronic acid were identified throughout the course of oocyte maturation (Figures 6E-6G; Figure S12A), indicative of active PPP. Moreover, 5/6 PPP-related enzymes we detected also showed statistically significant increase in level during meiotic maturation (Figures S12B-S12G). Of the two primary starting metabolites for the PPP, glyceraldehyde fell ~3-fold during meiotic maturation and sorbitol increased ~5-fold during meiotic resumption and then fell ~2-fold by MII arrest; the mechanistic and developmental significance of these changes deserves future study.

Downs *et al.* have demonstrated that the flux of glucose via PPP, rather than through glycolysis, influences meiotic resumption in mouse cumulus-oocyte complexes (Downs et al., 1998; Downs et al., 1996). To dissect the roles of PPP in oocyte itself, glucose-6-phosphate dehydrogenase (G6PD), the rate-limiting enzyme of PPP, was specifically depleted using G6pdx-targeting siRNA (siG6pdx) (Figures S12H-S12I). The maturation rate of siG6pdx oocytes decreased slightly but significantly compared with controls (Figure S12J). One major phenotype of siG6pdx oocytes was excessive reactive oxygen species (ROS) production (Figures S12K-S12L), implying the imbalance of redox homeostasis. Importantly, a developmental arrest was evident when the matured siG6pdx oocytes were fertilized *in vitro*, displaying a reduced proportion of on-time 2-cell embryo formation relative to controls (Figures S12M-S12N), indicative of an impaired oocyte to embryo transition. The knockdown phenotypes were restored by an mRNA rescue experiment, confirming the siG6pdx target specificity (Figures S12H-S12K). These findings clearly suggest that PPP is active during oocyte maturation and needed maternally for development to early embryos.

A progressive increase in nucleotide metabolism during oocyte maturation

Purine and pyrimidine nucleotides are major energy carriers, subunits of nucleic acids, and precursors for the synthesis of nucleotide cofactors such as nicotinamide adenine dinucleotide (NAD) and SAM (Moffatt and Ashihara, 2002). Ribulose 5-phosphate (R5P) is the end product of the oxidative reactions in PPP. The *de novo* synthesis of purine begins with the activation of R5P to phosphoribosyl pyrophosphate (PRPP), and ends with the production of inosine monophosphate (IMP). Consistent with the active PPP during maturation, the abundance of 7 out of 10 nucleotide-related metabolites increased during meiotic maturation (Figures 7A-7K); the increase was observed for both purines, particularly a ~14-fold increase in IMP, as well as for pyrimidine nucleotides, particularly a ~5-fold increase in cytidine. Correspondingly, integrated analysis of proteomics and metabolic pathways showed elevated levels of 17 out of 23 enzymes involved in nucleotide metabolism (Figures 7L-7P; Figures S14-S16). For instance, in matured oocytes, purine nucleoside phosphorylase (PNP), an enzyme in the purine salvage pathway, exhibited a 3–6-fold increase (Figure 7L); and dihydroorotate dehydrogenase (DHODH), a rate-limiting enzyme

in the *de novo* biosynthesis of pyrimidines, exhibited ~2-fold increase (Figure 7O). The increases in purine and pyrimidine levels likely provide maternal support for the large amount of DNA and RNA synthesis that will occur during early embryonic development. We also observed that levels of inosine and xanthosine significantly declined during oocyte maturation (Figures 7I-7J). Previous studies have implicated inosine and hypoxanthine in participation in the maintenance of mouse GV stage diplotene arrest (Downs et al., 1986; Eppig et al., 1985). The fall we observe presumably reflects the necessity to decreased levels of inosine and xanthosine to allow meiotic resumption. Collectively, these data indicate that nucleotide metabolism pathways are important participants in mechanisms regulating meiotic maturation.

DISCUSSION

In the present study, through the integrated analysis of metabolomics and proteomics, we have characterized the global metabolic patterns during *in vivo* oocyte maturation. Using functional approaches, we further identified the critical factors mediating the effects of PUFAs on oocyte meiosis, and discovered the control of epigenetic landscape in oocytes via SGOC pathway.

Metabolic patterns during oocyte maturation

For a long time, due to the scarcity of experimental material, oocyte metabolism has been investigated mainly by using radiolabelled substrates in combination with inhibitor treatment (Gu et al., 2015). Significant effort has focused on the utilization of exogenous substrates by oocytes at specific stage, but the dynamics of endogenous metabolites have not been extensively examined. Here, we therefore established temporal metabolome profiles during *in vivo* maturation. In parallel, we conducted quantitative proteomic studies to bolster the metabolomic data. Based on these integrated profiles, we clarify the metabolic basis illustrating the functions of the known pathways in oocytes. For instance, we observed that carnitine/palmityolcarnitine levels and CPTII accumulation are markedly increased upon meiotic resumption (Figure 2). This finding provides the potential explanation for why (*i*) CPT inhibition in mouse oocytes blocks meiotic resumption (Downs et al., 2009), and (*ii*) carnitine supplementation during *in vitro* culture improves both oocyte nuclear and cytoplasmic maturation (Dunning et al., 2011). Importantly, we discovered the metabolic characteristics during oocyte maturation, including (*i*) diminished bile acid biosynthesis; (*ii*) a sharp decline in PUFAs content; (*iii*) active one-carbon metabolism; and (*iv*) a progressive increase in the levels of a number of nucleotides. These dynamic changes in different pathways not only lay a foundation for comparative studies of abnormal oocyte development, but also could be used as metabolic signatures to predict oocyte quality and improve *in vitro* culture system for assisted reproduction.

Fatty acid regulation of oocyte development

In comparison with other macronutrient classes, fatty acids yield the most ATP by the FAO pathway. Elevated carnitine abundance (Figure 2) and active TCA cycle (Figure 6) strongly suggest that lipid metabolism participates in energy provision for oocyte maturation. The data imply that there is an increase in beta-oxidation, which is predicted to elevate the levels

of FADH2 and NADH. However, our metabolomics analysis did not detect either of them (Table S1). Similarly, tetrahydrofolate (TFH) in the folate cycle was not detected. Thus some of our inferences from changes in metabolite and metabolic enzyme levels should be considered as preliminary.

On the other hand, free fatty acids and their derivatives also act as signaling molecules that are released under tight developmental control. They are involved in various cellular processes through the modulation of gene transcription, protein modifications, and enzyme activities (Snaebjornsson et al., 2020). Here, we identified two targets of ARA inhibition that promote meiotic maturation (Figure 3). Our data suggest a model that ARA reduces NKAP/BTG4 abundance at GV stage, while the fall in ARA during meiotic resumption allows them to accumulate, promoting the assembly of meiotic apparatus and triggering the degradation of maternal RNAs, respectively. Future work is needed to address the mechanism through which high ARA suppresses NKAP/BTG4 protein accumulation during oocyte maturation. In addition, fat metabolism has been linked to reproductive development in animals and humans. For example, obese women often suffer from poor outcomes across the reproductive spectrum including early pregnancy loss, congenital abnormalities, and neonatal conditions (Broughton and Moley, 2017). Recently, we discovered that obesity induces the loss of Stella, a maternal factor, in oocytes, contributing to those reproductive disorders (Han et al., 2018). Hence, it is conceivable that environmental insults such as mal- or overnutrition may disrupt the metabolic patterns of fatty acids, particularly PUFAs, in the follicle niche, which in turn influences the abundance of critical factors in oocytes.

Metabolic control of epigenetic modifications in oocytes

It is now appreciated that a cell's metabolic state is integrated with epigenetic regulation. Many of the chemical modifications that decorate DNA and histones are adducts derived from intermediates of cellular metabolic pathways (Lu and Thompson, 2012). Epigenetic modifications are vulnerable to prenatal environmental exposures occurring during germ cell development. Assisted reproductive technologies (ART)-conceived infants have higher frequency of birth defects related to epigenetic changes, which is likely a consequence of sub-optimal culture condition *in vitro* (Canovas et al., 2017; El Hajj and Haaf, 2013). Epigenetic perturbations in germ cells might mediate the transgenerational effects of parental obesity (Bodden et al., 2020; Huypens et al., 2016). Nevertheless, direct evidence for metabolites involvement in epigenetic establishment during oogenesis is still lacking. Here, we not only showed the active SGOC metabolism during meiotic maturation, but also demonstrated that SAM produced from this pathway is used for establishing DNA methylation in MII oocytes and histone methylation in zygotes (Figure 5). Such a metabolic signature may represent a mechanistic basis for environmental effects on epigenetic marks in germ cells and embryos. Our study cannot exclude the possibility that the reduced genome methylation in siShmt2 oocytes might be a result of low cell fitness. Genetic manipulations of key metabolism-related genes are required to comprehensively understand the metabolic control of epigenetic modifications in oocyte development.

Limitations

A strength of our study is the description of *in vivo* oocyte metabolism during maturation. However, to carry out such metabolomic profiling ~3,200 mice were used to retrieve oocytes. Other parts of these mice (i.e., granulosa cells, muscle, liver, pancreas, bones, and adipose tissues) were simultaneously collected for different projects. In future, using a targeted extraction method and specific chromatography column would probably increase the metabolite coverage and reduce the number of mice used in similar studies. In addition, the datasets here were derived from superovulated oocytes, and hormone stimulation may influence oocyte metabolism. Although single-cell metabolomic analysis is still in its infancy, such an emerging technology is a promising tool to profile metabolites in naturally ovulated oocytes.

Oocytes cannot be fully understood in isolation from their follicles. Metabolic coupling between oocytes and the companion granulosa cells is essential for the functions of both compartments (Su et al., 2009). Thus, metabolomic profiling of granulosa cells will further our understanding of metabolic control of oocyte development. In addition, two questions are of significant interest for future study: (*i*) the function of other significantly altered metabolic pathways (i.e. bile acid/amino acid/nucleotide synthesis) in maturing oocytes; (*ii*) the inter-relationships between distinct metabolic patterns during oocyte maturation. There also exist potential weaknesses of current study: (*i*) The data we have obtained is steady-state metabolite level and does not provide information on flux through the pathway. However, flux studies are very challenging given the experimental constraints of analysis of oocyte meiosis, particularly the limited amount of material. We have inferred changes in flux based on alterations in levels of metabolites and the relevant metabolic enzymes. (*ii*) Changes in metabolism occur via alterations in level of metabolic enzymes as well as their activity, through allosteric regulation and protein modification. Here we only assessed enzyme abundance in oocytes, which perhaps partly explained the lack of strong correlation between the levels of enzymes and metabolites in certain metabolic pathways. (*iii*) Several inhibitors (i.e., curcumin and sesamin) were used in this study to evaluate the PUFA metabolism during oocyte maturation. Given that these compounds may not be specific for the intended enzymes, a cleaner way (i.e., knockdown or knockout) targeting the relevant pathways is needed to clarify this question.

In sum, we explored the dynamics of metabolome and proteome, leading to the characterization of metabolic patterns during oocyte maturation. Our dataset constructs a framework for future studies addressing the complex interplay between nutritional state and oocyte development. Additionally, these findings provide tremendous opportunities to predict oocyte quality and define better culture systems for human assisted reproduction.

STAR⋆METHODS

RESOURCE AVAILABILITY

Lead Contact—Further information and requests for reagents and resources should be directed to and will be fulfilled by the lead contact, Qiang Wang (qwang2012@njmu.edu.cn).

Materials Availability—All unique reagents generated in this study are available from the Lead Contact with a completed Materials Transfer Agreement.

Data and Code Availability—The accession number for the oocyte proteomic dataset reported in this paper is PRIDE: PXD018777 (username: reviewer55684@ebi.ac.uk; password: mYMGRG0w) and PXD018753 (username: reviewer43455@ebi.ac.uk; password: Uz92GHI2). The accession number for the oocyte Bisulfite-seq dataset reported in this paper is GEO: GSE149053.

Original data have been deposited to Mendeley Data: https://data.mendeley.com/datasets/8tftw77m4z/draft?a=f27e269e-9b60–43f2–9cc b-09c720c7a3bb.

EXPERIMENTAL MODEL AND SUBJECT DETAILS

Mouse.—All animal experiments follow the rules and guidelines of the local animal ethical committee and the Animal Care and Use Committee of Nanjing Medical University (Protocol NO. IACUC-1703017). C57BL/6 mice were purchased from Charles River Laboratories China Inc, and were housed in ventilated cages on a 12:12-h light-dark cycle at constant temperature (22°C) and under controlled humidity.

Oocyte collection and culture.—3-week old female mice were superovulated by injecting 5 units of pregnant mares serum gonadotropin (PMSG) followed by 5 units of human chorionic gonadotropin (hCG) 48h after PMSG priming. Mice were sacrificed by cervical dislocation 0, 3, or 12 hours post-hCG injection. To collect GV and GVBD oocytes, cumulus-oocyte complexes (COCs) were retrieved by manual rupturing of antral ovarian follicles, and cumulus cells were removed by repeatedly pipetting. To collect MII oocytes, COCs were isolated from oviduct ampullae, and cumulus masses were removed in medium containing 0.5 mg ml^{-1} hyaluronidase at 37°C. For *in vitro* maturation, fully grown GV oocytes were cultured in M16 medium under mineral oil at 37°C in a 5% CO2 incubator.

METHODS DETAILS

***In vitro* fertilization and embryo culture.—**IVF assays were conducted as we previously described (Han et al., 2018). In brief, sperm was obtained from dissected epididymis of C57BL/6 mice aged 10–20 weeks, and left to capacitate for one hour in HTF fertilization medium (Millipore, Merck, Germany) supplemented with 10 mg/ml bovine serum albumin (BSA). After fertilization in a 37°C incubator, zygotes were cultured in KSOM medium (Millipore, Merck, Germany) at 37°C in a humidified atmosphere of 5% CO2, 5% O2, 90% N2.

Treatment of oocytes with inhibitors and chemicals.—For treatment with inhibitors, INDO (Selleck Chemicals, TX, USA; Cat#: S5010), BWA4C (Sigma Aldrich, MO, USA; Cat#: B7559), Sesamin (Selleck Chemicals, TX, USA; Cat#: S2392), and Curcumin (Selleck Chemicals, TX, USA; Cat#: S1848) solutions were prepared in dimethyl sulfoxide (DMSO), and then diluted to yield a final concentration in maturation medium as needed. GV oocytes were *in vitro* cultured in M16 medium containing different doses of inhibitor for further analysis. Correspondingly, 0.1% DMSO was included as a control. To

assess the effects of PUFAs on oocyte maturation, fully grown GV oocytes were cultured in M16 medium supplemented with different concentrations of ARA, DHA, and EPA. The relevant phenotypes were examined at the indicated time points.

siRNA knockdown.—Microinjection of siRNAs, with a Narishige microinjector, was used for knockdown analysis in mouse oocytes. Nkap- and Shmt2-siRNAs purchased from GenePharma (Shanghai, China) were diluted with water to give a stock concentration of 20 μM, and approximately 2.5 pl of solution was injected. The same volume of general negative control siRNA was injected as control. In order to facilitate the siRNA-mediated knockdown, oocytes were arrested at GV stage in M16 medium containing 2.5 μM milrinone for more than 7 hours, and then cultured in normal medium for further experiments. To confirm the specificity of siRNA knockdown, mRNA rescue experiments were performed as we described previously (Zhang et al., 2017), where the Nkap/Shmt2/G6pdx encoding cRNA contains mutations insensitive to the siRNA. To obtain the rescue construct for siRNA, several wobble codon mutations in the central siRNA-binding region were introduced by overlapping PCR. The majority of rescue oocytes could progress through meiosis II, and present the normal phenotypes as controls (Figure S13). These results demonstrate that the defects caused by the siRNA knockdown are specific. siRNAs and the relevant primer sequences are listed in Table S4.

Overexpression analysis.—*In vitro* synthesis of cRNA was conducted as we described previously (Hou et al., 2015). In brief, total RNA was extracted from 100 oocytes using Arcturus PicoPure RNA Isolation Kit (Applied Biosystems, CA, USA), and cDNA was generated using Quantitect Reverse Transcription Kit (Qiagen, Germany). Full length PCR products were cloned into the $pCS2^{+}$ vector with six Myc tags. Capped cRNAs were made via *in vitro* transcription using SP6 mMESSAGE mMACHINE (Ambion, CA, USA). For overexpression experiments, approximately 5–10 pl of cRNA (1,000 ng/μl) was microinjected into fully grown oocytes. The primer sequences are listed in Table S4.

Western blotting.—A pool of denuded oocytes was lysed in Laemmli sample buffer containing protease inhibitor and then subjected to SDS-PAGE. The separated proteins were transferred to a polyvinylidene fluoride (PVDF) membrane. The membranes were blocked in TBS containing 0.1% Tween 20 and 5% low fat dry milk for one hour and then incubated with primary antibodies. Following incubation with HRP-conjugated secondary antibodies, the protein bands were visualized via Pierce ECL western blotting substrate (Thermo Fisher Scientific, Rockford, IL) according to the manufacturer's instructions.

Immunofluorescence.—Oocytes/embryos were fixed with 4% paraformaldehyde for 30 minutes and permeabilizedwith 0.5% Triton X-100 for 20 minutes. Following blocking in 1% BSA-supplemented PBS for 1 hour, samples were incubated overnight at 4°C with primary antibodies as follows: anti-NKAP antibody, anti-H3K4me3 antibody, anti-BubR1 antibody, and FITC-conjugated anti-tubulin antibody. To detect kinetochores, oocytes were co-labeled with CREST according to our previous protocol (Ma et al., 2014). Chromosomes were stained with propidium iodide (red) or Hoechst 33342 (blue) for 15 minutes. After several washes, samples were mounted on anti-fade medium (Vectashield, Burlingame, CA,

USA) and examined under a Laser Scanning Confocal Microscope (LSM 710, Zeiss, Germany). The intensity of fluorescence was measured and quantified using Image J software (NIH), as we described previously (Han et al., 2018; Ma et al., 2014).

ROS evaluation.—Intracellular ROS levels were determined by CM-H2DCFDA (Life Technologies, Invitrogen TM, Cat#: C6827) according to our protocol (Wang et al., 2018). CM-H2DCFDA was prepared in DMSO prior to loading. Oocytes were incubated in culture medium containing 5 mM CM-H2DCFDA for 30 minutes at 37°C. Following three washes, 5–10 oocytes were transferred to a live cell-imaging dish, and then immediately observed using Laser Scanning Confocal Microscope (LSM 710, Zeiss, Germany).

Quantitative real-time PCR.—mRNA level was analyzed by quantitative real-time PCR (qRT-PCR) as we reported previously (Hou et al., 2015). Total RNA was isolated from 50 oocytes using Arcturus PicoPure RNA Isolation Kit (Applied Biosystems, CA, USA) and first-strand cDNA was generated using a cDNA Synthesis Kit (Qiagen, Germany). Real-time PCR was performed with SYBR Green using an ABI StepOnePlus Real-time PCR system (Applied Biosystems, CA, USA). Glyceraldehydes-3-phosphate dehydrogenase (Gapdh) was used as an internal control. Experiments were performed at least in triplicate. Primer sequences are listed in Table S4.

Poly (A) tail assay.—Poly (A) tail (PAT) assay was conducted according to the published protocol (Yu et al., 2016) with minor modifications. In brief, total RNA was isolated from 200 oocytes at the indicated time points using Arcturus PicoPure RNA Isolation Kit (Applied Biosystems, CA, USA). Primer P1 (5'-P-GGTCACCTTGATCTGAAGC-NH2–3') was anchored to RNA by T4 RNA ligase. Reverse transcription was performed using a SuperScript III First-Strand Synthesis SuperMix (Life Technologies, Invitrogen TM, Cat#: 18080–400) with the P1-antisense primer P2 (5'-GCTTCAGATCAAGGTGACCTTTTT-3'), and then products were amplified by PCR with gene-specific primers and primer P2. The PCR conditions were as follows: 30 s at 94 °C, 30 s at 50 °C, and 50 s at 72 °C for 35 cycles, and products were analyzed on a 2.5% agarose gel. Primer sequences are listed in Table S4.

Metabolomics.—GV, GVBD, and MII oocytes were harvested separately from ~3,200 mice (2,000 oocytes per sample, 9 samples for each stage). Samples were transferred to Eppendorf tubes, immediately flash frozen in liquid nitrogen, and then stored at −80 °C. For metabolite extraction, samples were resuspended in 300 μL of 80% methanol/water (vol/vol) and homogenized using an Ultra-Turrax homogenizer. After cooling on ice for 10 min, samples were spun at 16,000g for 15 min at 4 °C. Supernatant (250 μL per sample) was transferred to a new tube, and dried samples were stored at −80 °C until instrumental analysis. The metabolomics data were collected using a standard metabolic profiling method we previously described (Huang et al., 2019; Zhang et al., 2020). Briefly, experiments were performed on an UPLC Ultimate 3000 system (Dionex, Germering, Germany) coupled to a Q-Exactive mass spectrometer (Thermo Fisher Scientific, Bremen, Germany). Each sample was injected for analysis in a randomized fashion to avoid complications related to the injection order. The chromatographic separation was conducted using Hypersil GOLD C18

column (100 mm × 2.1 mm, 1.9 μm) (Thermo Fisher Scientific) with temperature set at 40 °C. The mobile phase consists of phase A (0.1% formic acid in ultra-pure water) and B (0.1% formic acid in pure ACN), which was run at a flow rate of 0.4 mL/min. After the initial 3-min elution of 99% (vol/vol) A, the percentage of solvent A gradually decreased to 1% (vol/vol) at t = 10 min. The composition of solvent A was maintained at 1% (vol/vol) for 3 min (t = 13 min), and then immediately increased to 99% (vol/vol) lasting for 2 min (t = 15 min). The mass spectrometer was performed in a full-scan mode ranging from 70 m/z to 1050 m/z, running at a 70,000 resolution in both positive and negative modes simultaneously.

Raw data acquired by the mass spectrometer were submitted to TraceFinder (v3.1). The metabolite identification was conducted by the comparison of accurate mass and retention time with the commercial standard compounds using the author-constructed library. Similar procedure was used to detect specific metabolites (ARA, DHA, EPA, serine, glycine, and SAM). All statistical analyses were performed using "R" (V2.15). Student's *t* test was used to compare continuous variables between two groups (Kim, 2015). SIMCA-P software (V14.0; Umetrics AB, Umea, Sweden) was employed for OPLS-DA. The variable importance in projection (VIP) value > 1.00 and P value < 0.05 of each metabolite were used as the combined cut-offs of the statistical significance. The integration and visualization of metabolomics and proteomics data were conducted with the KEGG Mapper (V4.1) (https://www.genome.jp/kegg/).

Proteomics.—GV, GVBD, and MII oocytes collected from normal mice were lysed in urea lysis buffer (8 M urea, 75 mM NaCl, 50 mM Tris, pH 8.2, 1% (v/v) EDTA-free protease inhibitor, 1 mM NaF, 1 mM β-glycerophosphate, 1 mM sodiumorthovanadate, 10 mM sodium pyrophosphate, 1 mM PMSF) and subjected to centrifugation at 40,000 g for 1h. Proteins were prepared and trypsin digested as we described before (Liu et al., 2019). Following digestion, the purified peptides were subjected to the 6-plex tandem mass tag (TMT) labeling according to previously published methods (Liu et al., 2019). Peptides from two replicates of three stages of oocytes (375 oocytes for one replicate of each stage of oocytes) were labeled with respective isobaric tags and mixed together. Two labeling experiments were performed for the total four replicates of each stage of oocytes. To improve the coverage of protein identification and quantification, the mixed TMT-labeled peptides were separated by the high-pH reversed phase (HP-RP) fractionation technology based on the ACQUITY® UPLC M-class system (Waters) with an BEH C18 Column (300 μm×150 mm, 1.7 μm; Waters), and a total of 30 fractions were collected and lyophilized for each experiment. Arachidonic acid (ARA) treated and control oocytes in 3 replicates were subjected to the 6-plex TMT labeling using the similar method described above, except that a total of 20 fractions were collected in HP-RP fractionation. All fractions were analyzed by LC-MS/MS using an UltiMateTM 3000 RSLCnano HPLC system coupled through a nanoelectrospray source to LTQ Orbitrap Velos mass spectrometer (Thermo Fisher Scientific, San Jose, CA). Peptides were separated with a trap column (75 μm×2 cm, Acclaim® PepMap100 C18 column, 3 μm, 100 Å; Thermo Fisher Scientific) and an analytical column (75 μm×25 cm, Acclaim® PepMap RSLC C18 column, 2 μm, 100 Å; Thermo Fisher Scientific) at 300 nl/min using a 194-min gradient (3% to 5% buffer B for 3

min, 5% to 30% buffer B for 167min, 30% to 45% buffer B for 15 min, 45% to 99% buffer B for 1 min, 99% buffer B for 8 min). The parameter settings for mass spectrometer were referred to our published reports (Castaneda et al., 2017; Wang et al., 2017).

The MaxQuant software (V1.2.2.5) was used for searching the raw files against UniProt mouse proteome database (Cox and Mann, 2008). The FDR of identified peptides and proteins was set to 1%. Precursor mass tolerance was set to 20 ppm and product ions were searched with a mass tolerance 0.5 Da. Searches were performed using Trypsin/P enzyme specificity while allowing up to two missed cleavages. TMT tags on lysine residues and peptide N-termini (+229.1629 Da) and carbamidomethylation of cysteine residues (+57.0215 Da) were set as fixed modifications. Variable modifications included oxidation of methionines and acetylation of protein N termini. Peptides and proteins with FDR ≤ 1% were considered confident, and proteins with at least one unique peptide were subjected to quantitative analysis. Relative expression values for each protein were calculated by combining MaxQuant identification results with a local modified Libra algorithm (Guo et al., 2018; Wang et al., 2017; Wen et al., 2016). The labeling efficiency was evaluated using the first HP-RP fraction of each TMT experiment with MaxQuant software except that TMT tags on lysine residues and peptide N-termini (+229.1629 Da) were set as optional modifications (Zecha et al., 2019). The efficiency is 98.2% and 98.5% for the two labeling replicates of GV/GVBD/MII oocytes, and 99.1% for ARA/control oocytes, respectively.

For GV, GVBD, and MII oocytes, Student's *t* test adjusted by FDR was performed using Perseus (Tyanova et al., 2016) to calculate significant differences in abundances between groups. A volcano plot was constructed to better visualize and identify the differentially expressed proteins between groups. Heat map was produced accompanied by a dendrogram depicting the extent of similarity of protein expression among the samples. For the convenience of gene annotation, corresponding Ensembl gene IDs of the differentially expressed proteins were used for further bioinformatics analysis. To characterize these genes, enrichment of Kyoto Encyclopedia of Genes and Genomes (KEGG) pathways was analyzed by using DAVIDs Functional Annotation Chart tool (V6.8) (Huang da et al., 2009). A FDR-q value less than 0.05 was controlled for significant enrichment. Pathway Studio (V6.00) software (Ariadne Genomics, MD, USA) (Nikitin et al., 2003) was used to identify the cellular processes regulated by the differential proteins confirmed via the PubMed/Medline hyperlink embedded in each node. The network between proteins and cellular processes was constructed using Cytoscape (Shannon et al., 2003).

Oocyte methylome profiling.—The DNA methylome for MII oocytes were analysed, as we described before (Han et al., 2018). In brief, denuded oocytes (30 oocytes for each sample) were lysed in lysis buffer (10 mM Tris-Cl pH 7.4 and 2% SDS) with 0.5 μl protease K for 1 h at 37 °C. Bisulfite conversion was performed on cell lysates using the EZ DNA Methylation-Gold Kit (Zymo Research), and then the converted DNA was processed for library construction. The quality and quantity of the purified library were evaluated by employing Agilent Bioanalyzer and StepOnePlus Real-Time PCR System (Applied Biosystems). Libraries were prepared for 125-bp paired-end sequencing on a HiSeq2500.

Cleaned data was obtained by removing poor-quality bases and adapter sequences of raw sequencing reads using Trim Galore. Bismark (Krueger and Andrews, 2011) was used to map cleaned data to the mouse genome assembly (GRCm38) with parameters '*paired mode, options –non-directional,-bam,--bowtie2*'. CG methylation calls from uniquely mapped reads were analyzed using probes designed across genomic features that were defined as follows. CpG islands (CGIs) were extracted from the CpG islands track of the UCSC Genome Browser (Speir et al., 2016), and CGI shores were defined as the regions 2kb around from the CGI. Promoters were defined as the region 2kb upstream from TSSs (transcriptional start sites) annotated by UCSC RefSeq (O'Leary et al., 2016). Exons, introns, UTRs, and intergenic regions were defined according to annotation of UCSC RefSeq. All repeat elements were extracted from the Repeatmasker track of the UCSC Genome Browser. To test whether low complexity regions (LCRs) CEL were differentially methylated between two groups, metilene was used with default parameters. The distribution of LCRs across the whole genome was determined by overlapping with the RefSeq annotation using BEDOPS with default parameters. The enrichment of differentially methylated LCRs in whole genome was calculated with Fisher exact test.

Quantification and statistical analysis.—All experiments were repeated three times with similar results, and data from one representative experiment are shown unless otherwise stated. All analyses were performed using GraphPad Prism (V7.0) for Windows. Statistical comparisons were made with Student's *t* test, Fisher exact test, and Bootstrap test when appropriate. Data are presented as mean value ± SD. Changes were considered statistically significant when $P < 0.05$.

Supplementary Material

Refer to Web version on PubMed Central for supplementary material.

ACKNOWLEDGEMENTS

This work was supported by National Key Scientific Research Projects (NO. 2017YFC1001500 and 2018YFC1004000 to Q.W.; 2016YFA0503300 to X.G.), National Natural Science Foundation of China (NO. 81925014 and 31771657 to Q.W.; NO. 81872650 to M.C.), Science Foundation for Distinguished Young Scholars of Jiangsu Province (BK20180035 to Q.W.), and United States NIH grant (R01GM100756 to T.S.).

Li et al. reveals the metabolic framework that supports *in vivo* oocyte maturation via the integrated analysis of metabolomics and proteomics, providing a broad resource for probing mammalian oocyte metabolism.

1 Established the temporal metabolome and proteome profiles of mouse oocytes

2 Discovered metabolic features during oocyte maturation

3 Identified key targets mediating the action of PUFA on meiotic maturation

4 Demonstrated the control of epigenetic marks in maturing oocytes by SGOC network

REFERENCES

Biggers JD, Whittingham DG, and Donahue RP (1967). The Pattern of Energy Metabolism in the Mouse Oocyte and Zygote. Proc Natl Acad Sci U S A 58, 560–567. [PubMed: 5233459]

Bodden C, Hannan AJ, and Reichelt AC (2020). Diet-Induced Modification of the Sperm Epigenome Programs Metabolism and Behavior. Trends Endocrinol Metab 31, 131–149. [PubMed: 31744784]

Broughton DE, and Moley KH (2017). Obesity and Female Infertility: Potential Mediators of Obesity's Impact. Fertil Steril 107, 840–847. [PubMed: 28292619]

Brunet S, Pahlavan G, Taylor S, and Maro B (2003). Functionality of the Spindle Checkpoint During the First Meiotic Division of Mammalian Oocytes. Reproduction 126, 443–450. [PubMed: 14525526]

Burgute BD, Peche VS, Steckelberg AL, Glockner G, Gassen B, Gehring NH, and Noegel AA (2014). Nkap Is a Novel Rs-Related Protein That Interacts with Rna and Rna Binding Proteins. Nucleic Acids Res 42, 3177–3193. [PubMed: 24353314]

Canovas S, Ivanova E, Romar R, Garcia-Martinez S, Soriano-Ubeda C, Garcia-Vazquez FA, Saadeh H, Andrews S, Kelsey G, and Coy P (2017). DNA Methylation and Gene Expression Changes Derived from Assisted Reproductive Technologies Can Be Decreased by Reproductive Fluids. Elife 6.

Castaneda JM, Hua R, Miyata H, Oji A, Guo Y, Cheng Y, Zhou T, Guo X, Cui Y, Shen B, et al. (2017). Tcte1 Is a Conserved Component of the Dynein Regulatory Complex and Is Required for Motility and Metabolism in Mouse Spermatozoa. Proc Natl Acad Sci U S A 114, E5370–E5378. [PubMed: 28630322]

Chen J, Melton C, Suh N, Oh JS, Horner K, Xie F, Sette C, Blelloch R, and Conti M (2011). Genome-Wide Analysis of Translation Reveals a Critical Role for Deleted in Azoospermia-Like (Dazl) at the Oocyte-to-Zygote Transition. Genes Dev 25, 755–766. [PubMed: 21460039]

Cox J, and Mann M (2008). Maxquant Enables High Peptide Identification Rates, Individualized P.P.B.-Range Mass Accuracies and Proteome-Wide Protein Quantification. Nat Biotechnol 26, 1367–1372. [PubMed: 19029910]

de Aguiar Vallim TQ, Tarling EJ, and Edwards PA (2013). Pleiotropic Roles of Bile Acids in Metabolism. Cell Metab 17, 657–669. [PubMed: 23602448]

Downs SM, Coleman DL, and Eppig JJ (1986). Maintenance of Murine Oocyte Meiotic Arrest: Uptake and Metabolism of Hypoxanthine and Adenosine by Cumulus Cell-Enclosed and Denuded Oocytes. Dev Biol 117, 174–183. [PubMed: 2875006]

Downs SM, Humpherson PG, and Leese HJ (1998). Meiotic Induction in Cumulus Cell-Enclosed Mouse Oocytes: Involvement of the Pentose Phosphate Pathway. Biol Reprod 58, 1084–1094. [PubMed: 9546744]

Downs SM, Humpherson PG, Martin KL, and Leese HJ (1996). Glucose Utilization During Gonadotropin-Induced Meiotic Maturation in Cumulus Cell-Enclosed Mouse Oocytes. Mol Reprod Dev 44, 121–131. [PubMed: 8722700]

Downs SM, and Mastropolo AM (1994). The Participation of Energy Substrates in the Control of Meiotic Maturation in Murine Oocytes. Dev Biol 162, 154–168. [PubMed: 8125183]

Downs SM, Mosey JL, and Klinger J (2009). Fatty Acid Oxidation and Meiotic Resumption in Mouse Oocytes. Mol Reprod Dev 76, 844–853. [PubMed: 19455666]

Dunning KR, Akison LK, Russell DL, Norman RJ, and Robker RL (2011). Increased Beta-Oxidation and Improved Oocyte Developmental Competence in Response to L-Carnitine During Ovarian in Vitro Follicle Development in Mice. Biol Reprod 85, 548–555. [PubMed: 21613630]

Dunning KR, Cashman K, Russell DL, Thompson JG, Norman RJ, and Robker RL (2010). Beta-Oxidation Is Essential for Mouse Oocyte Developmental Competence and Early Embryo Development. Biol Reprod 83, 909–918. [PubMed: 20686180]

El Hajj N, and Haaf T (2013). Epigenetic Disturbances in in Vitro Cultured Gametes and Embryos: Implications for Human Assisted Reproduction. Fertil Steril 99, 632–641. [PubMed: 23357453]

Eppig JJ (1976). Analysis of Mouse Oogenesis in Vitro. Oocyte Isolation and the Utilization of Exogenous Energy Sources by Growing Oocytes. J Exp Zool 198, 375–382. [PubMed: 1003146]

Eppig JJ, Ward-Bailey PF, and Coleman DL (1985). Hypoxanthine and Adenosine in Murine Ovarian Follicular Fluid: Concentrations and Activity in Maintaining Oocyte Meiotic Arrest. Biol Reprod 33, 1041–1049. [PubMed: 4074802]

Fagbohun CF, and Downs SM (1992). Requirement for Glucose in Ligand-Stimulated Meiotic Maturation of Cumulus Cell-Enclosed Mouse Oocytes. J Reprod Fertil 96, 681–697. [PubMed: 1339848]

Ferguson EM, and Leese HJ (1999). Triglyceride Content of Bovine Oocytes and Early Embryos. J Reprod Fertil 116, 373–378. [PubMed: 10615263]

Ferguson EM, and Leese HJ (2006). A Potential Role for Triglyceride as an Energy Source During Bovine Oocyte Maturation and Early Embryo Development. Mol Reprod Dev 73, 1195–1201. [PubMed: 16804881]

Goni FM, Requero MA, and Alonso A (1996). Palmitoylcarnitine, a Surface-Active Metabolite. FEBS Lett 390, 1–5. [PubMed: 8706815]

Gu L, Liu H, Gu X, Boots C, Moley KH, and Wang Q (2015). Metabolic Control of Oocyte Development: Linking Maternal Nutrition and Reproductive Outcomes. Cell Mol Life Sci 72, 251–271. [PubMed: 25280482]

Guo J, Zhang T, Guo Y, Sun T, Li H, Zhang X, Yin H, Cao G, Yin Y, Wang H, et al. (2018). Oocyte Stage-Specific Effects of Mtor Determine Granulosa Cell Fate and Oocyte Quality in Mice. Proc Natl Acad Sci U S A 115, E5326–E5333. [PubMed: 29784807]

Han L, Ren C, Li L, Li X, Ge J, Wang H, Miao YL, Guo X, Moley KH, Shu W, et al. (2018). Embryonic Defects Induced by Maternal Obesity in Mice Derive from Stella Insufficiency in Oocytes. Nat Genet 50, 432–442. [PubMed: 29459681]

Harris SE, Adriaens I, Leese HJ, Gosden RG, and Picton HM (2007). Carbohydrate Metabolism by Murine Ovarian Follicles and Oocytes Grown in Vitro. Reproduction 134, 415–424. [PubMed: 17709560]

Homa ST, Racowsky C, and McGaughey RW (1986). Lipid Analysis of Immature Pig Oocytes. J Reprod Fertil 77, 425–434. [PubMed: 3735242]

Hou X, Zhang L, Han L, Ge J, Ma R, Zhang X, Moley K, Schedl T, and Wang Q (2015). Differing Roles of Pyruvate Dehydrogenase Kinases During Mouse Oocyte Maturation. J Cell Sci 128, 2319–2329. [PubMed: 25991547]

Huang da W, Sherman BT, and Lempicki RA (2009). Systematic and Integrative Analysis of Large Gene Lists Using David Bioinformatics Resources. Nat Protoc 4, 44–57. [PubMed: 19131956]

Huang Z, Xu B, Huang X, Zhang Y, Yu M, Han X, Song L, Xia Y, Zhou Z, Wang X, et al. (2019). Metabolomics Reveals the Role of Acetyl-L-Carnitine Metabolism in Gamma-Fe2o3 Np-Induced Embryonic Development Toxicity Via Mitochondria Damage. Nanotoxicology 13, 204–220. [PubMed: 30663479]

Hunt PA, and Hassold TJ (2008). Human Female Meiosis: What Makes a Good Egg Go Bad? Trends Genet 24, 86–93. [PubMed: 18192063]

Huypens P, Sass S, Wu M, Dyckhoff D, Tschöp M, Theis F, Marschall S, Hrabě de Angelis M, and Beckers J (2016). Epigenetic Germline Inheritance of Diet-Induced Obesity and Insulin Resistance. Nat Genet 48, 497–499. [PubMed: 26974008]

Kim TK (2015). T Test as a Parametric Statistic. Korean J Anesthesiol 68, 540–546. [PubMed: 26634076]

Krueger F, and Andrews SR (2011). Bismark: A Flexible Aligner and Methylation Caller for Bisulfite-Seq Applications. Bioinformatics 27, 1571–1572. [PubMed: 21493656]

Leese HJ (2015). History of Oocyte and Embryo Metabolism. Reprod Fertil Dev 27, 567–571. [PubMed: 25695313]

Leese HJ, and Barton AM (1985). Production of Pyruvate by Isolated Mouse Cumulus Cells. J Exp Zool 234, 231–236. [PubMed: 3998681]

Li T, Chen L, Cheng J, Dai J, Huang Y, Zhang J, Liu Z, Li A, Li N, Wang H, et al. (2016). Sumoylated Nkap Is Essential for Chromosome Alignment by Anchoring Cenp-E to Kinetochores. Nat Commun 7, 12969. [PubMed: 27694884]

Liu HB, Muhammad T, Guo Y, Li MJ, Sha QQ, Zhang CX, Liu H, Zhao SG, Zhao H, Zhang H, et al. (2019). Rna-Binding Protein Igf2bp2/Imp2 Is a Critical Maternal Activator in Early Zygotic Genome Activation. Adv Sci (Weinh) 6, 1900295.

Loewenstein JE, and Cohen AI (1964). Dry Mass, Lipid Content and Protein Content of the Intact and Zona-Free Mouse Ovum. J Embryol Exp Morphol 12, 113–121. [PubMed: 14155399]

Lu C, and Thompson CB (2012). Metabolic Regulation of Epigenetics. Cell Metab 16, 9–17. [PubMed: 22768835]

Ma R, Hou X, Zhang L, Sun SC, Schedl T, Moley K, and Wang Q (2014). Rab5a Is Required for Spindle Length Control and Kinetochore-Microtubule Attachment During Meiosis in Oocytes. FASEB J 28, 4026–4035. [PubMed: 24876181]

MacFarlane AJ, Liu X, Perry CA, Flodby P, Allen RH, Stabler SP, and Stover PJ (2008). Cytoplasmic Serine Hydroxymethyltransferase Regulates the Metabolic Partitioning of Methylenetetrahydrofolate but Is Not Essential in Mice. J Biol Chem 283, 25846–25853. [PubMed: 18644786]

Maddocks OD, Labuschagne CF, Adams PD, and Vousden KH (2016). Serine Metabolism Supports the Methionine Cycle and DNA/Rna Methylation through De Novo Atp Synthesis in Cancer Cells. Mol Cell 61, 210–221. [PubMed: 26774282]

McEvoy TG, Coull GD, Broadbent PJ, Hutchinson JS, and Speake BK (2000). Fatty Acid Composition of Lipids in Immature Cattle, Pig and Sheep Oocytes with Intact Zona Pellucida. J Reprod Fertil 118, 163–170. [PubMed: 10793638]

Mertens KL, Kalsbeek A, Soeters MR, and Eggink HM (2017). Bile Acid Signaling Pathways from the Enterohepatic Circulation to the Central Nervous System. Front Neurosci 11, 617. [PubMed: 29163019]

Moffatt BA, and Ashihara H (2002). Purine and Pyrimidine Nucleotide Synthesis and Metabolism. Arabidopsis Book 1, e0018.

Momb J, Lewandowski JP, Bryant JD, Fitch R, Surman DR, Vokes SA, and Appling DR (2013). Deletion of Mthfd1l Causes Embryonic Lethality and Neural Tube and Craniofacial Defects in Mice. Proc Natl Acad Sci U S A 110, 549–554. [PubMed: 23267094]

Nezi L, and Musacchio A (2009). Sister Chromatid Tension and the Spindle Assembly Checkpoint. Curr Opin Cell Biol 21, 785–795. [PubMed: 19846287]

Nikitin A, Egorov S, Daraselia N, and Mazo I (2003). Pathway Studio--the Analysis and Navigation of Molecular Networks. Bioinformatics 19, 2155–2157. [PubMed: 14594725]

O'Leary NA, Wright MW, Brister JR, Ciufo S, Haddad D, McVeigh R, Rajput B, Robbertse B, Smith-White B, Ako-Adjei D, et al. (2016). Reference Sequence (Refseq) Database at Ncbi: Current Status, Taxonomic Expansion, and Functional Annotation. Nucleic Acids Res 44, D733–745. [PubMed: 26553804]

Pasternak M, Pfender S, Santhanam B, and Schuh M (2016). The Btg4 and Caf1 Complex Prevents the Spontaneous Activation of Eggs by Deadenylating Maternal Mrnas. Open Biol 6.

Reina-Campos M, Diaz-Meco MT, and Moscat J (2020). The Complexity of the Serine Glycine One-Carbon Pathway in Cancer. J Cell Biol 219.

Risal S, Pei Y, Lu H, Manti M, Fornes R, Pui HP, Zhao Z, Massart J, Ohlsson C, Lindgren E, et al. (2019). Prenatal Androgen Exposure and Transgenerational Susceptibility to Polycystic Ovary Syndrome. Nat Med 25, 1894–1904. [PubMed: 31792459]

Saito T, Hiroi M, and Kato T (1994). Development of Glucose Utilization Studied in Single Oocytes and Preimplantation Embryos from Mice. Biol Reprod 50, 266–270. [PubMed: 8142545]

Sha QQ, Zhang J, and Fan HY (2019). A Story of Birth and Death: Mrna Translation and Clearance at the Onset of Maternal-to-Zygotic Transition in Mammalsdagger. Biol Reprod 101, 579–590. [PubMed: 30715134]

Shannon P, Markiel A, Ozier O, Baliga NS, Wang JT, Ramage D, Amin N, Schwikowski B, and Ideker T (2003). Cytoscape: A Software Environment for Integrated Models of Biomolecular Interaction Networks. Genome Res 13, 2498–2504. [PubMed: 14597658]

Smallwood SA, Tomizawa S, Krueger F, Ruf N, Carli N, Segonds-Pichon A, Sato S, Hata K, Andrews SR, and Kelsey G (2011). Dynamic Cpg Island Methylation Landscape in Oocytes and Preimplantation Embryos. Nat Genet 43, 811–814. [PubMed: 21706000]

Snaebjornsson MT, Janaki-Raman S, and Schulze A (2020). Greasing the Wheels of the Cancer Machine: The Role of Lipid Metabolism in Cancer. Cell Metab 31, 62–76. [PubMed: 31813823]

Speir ML, Zweig AS, Rosenbloom KR, Raney BJ, Paten B, Nejad P, Lee BT, Learned K, Karolchik D, Hinrichs AS, et al. (2016). The Ucsc Genome Browser Database: 2016 Update. Nucleic Acids Res 44, D717–725. [PubMed: 26590259]

Su YQ, Sugiura K, and Eppig JJ (2009). Mouse Oocyte Control of Granulosa Cell Development and Function: Paracrine Regulation of Cumulus Cell Metabolism. Semin Reprod Med 27, 32–42. [PubMed: 19197803]

Sutton-McDowall ML, Gilchrist RB, and Thompson JG (2010). The Pivotal Role of Glucose Metabolism in Determining Oocyte Developmental Competence. Reproduction 139, 685–695. [PubMed: 20089664]

Tani H, Ohnishi S, Shitara H, Mito T, Yamaguchi M, Yonekawa H, Hashizume O, Ishikawa K, Nakada K, and Hayashi JI (2018). Mice Deficient in the Shmt2 Gene Have Mitochondrial Respiration Defects and Are Embryonic Lethal. Sci Rep 8, 425. [PubMed: 29323231]

Tyanova S, Temu T, Sinitcyn P, Carlson A, Hein MY, Geiger T, Mann M, and Cox J (2016). The Perseus Computational Platform for Comprehensive Analysis of (Prote) Omics Data. Nat Methods 13, 731–740. [PubMed: 27348712]

Vrablik TL, and Watts JL (2013). Polyunsaturated Fatty Acid Derived Signaling in Reproduction and Development: Insights from Caenorhabditis Elegans and Drosophila Melanogaster. Mol Reprod Dev 80, 244–259. [PubMed: 23440886]

Wang H, Cheng Q, Li X, Hu F, Han L, Zhang H, Li L, Ge J, Ying X, Guo X, et al. (2018). Loss of Tigar Induces Oxidative Stress and Meiotic Defects in Oocytes from Obese Mice. Mol Cell Proteomics 17, 1354–1364. [PubMed: 29776966]

Wang M, Guo Y, Wang M, Zhou T, Xue Y, Du G, Wei X, Wang J, Qi L, Zhang H, et al. (2017). The Glial Cell-Derived Neurotrophic Factor (Gdnf)-Responsive Phosphoprotein Landscape Identifies Raptor Phosphorylation Required for Spermatogonial Progenitor Cell Proliferation. Mol Cell Proteomics 16, 982–997. [PubMed: 28408662]

Wang Q, and Sun QY (2007). Evaluation of Oocyte Quality: Morphological, Cellular and Molecular Predictors. Reprod Fertil Dev 19, 1–12.

Wen FP, Guo YS, Hu Y, Liu WX, Wang Q, Wang YT, Yu HY, Tang CM, Yang J, Zhou T, et al. (2016). Distinct Temporal Requirements for Autophagy and the Proteasome in Yeast Meiosis. Autophagy 12, 671–688. [PubMed: 27050457]

Yesilaltay A, Dokshin GA, Busso D, Wang L, Galiani D, Chavarria T, Vasile E, Quilaqueo L, Orellana JA, Walzer D, et al. (2014). Excess Cholesterol Induces Mouse Egg Activation and May Cause Female Infertility. Proc Natl Acad Sci U S A 111, E4972–4980. [PubMed: 25368174]

Yu B, Dong X, Gravina S, Kartal O, Schimmel T, Cohen J, Tortoriello D, Zody R, Hawkins RD, and Vijg J (2017). Genome-Wide, Single-Cell DNA Methylomics Reveals Increased Non-Cpg Methylation During Human Oocyte Maturation. Stem Cell Reports 9, 397–407. [PubMed: 28648898]

Yu C, Ji SY, Sha QQ, Dang Y, Zhou JJ, Zhang YL, Liu Y, Wang ZW, Hu B, Sun QY, et al. (2016). Btg4 Is a Meiotic Cell Cycle-Coupled Maternal-Zygotic-Transition Licensing Factor in Oocytes. Nat Struct Mol Biol 23, 387–394. [PubMed: 27065194]

Zecha J, Satpathy S, Kanashova T, Avanessian SC, Kane MH, Clauser KR, Mertins P, Carr SA, and Kuster B (2019). Tmt Labeling for the Masses: A Robust and Cost-Efficient, in-Solution Labeling Approach. Mol Cell Proteomics 18, 1468–1478. [PubMed: 30967486]

Zhang H, Lu T, Feng Y, Sun X, Yang X, Zhou K, Sun R, Wang Y, Wang X, and Chen M (2020). A Metabolomic Study on the Gender-Dependent Effects of Maternal Exposure to Fenvalerate on Neurodevelopment in Offspring Mice. Sci Total Environ 707, 136130. [PubMed: 31869608]

Zhang J, Ma R, Li L, Wang L, Hou X, Han L, Ge J, Li M, and Wang Q (2017). Intersectin 2 Controls Actin Cap Formation and Meiotic Division in Mouse Oocytes through the Cdc42 Pathway. FASEB J 31, 4277–4285. [PubMed: 28626024]

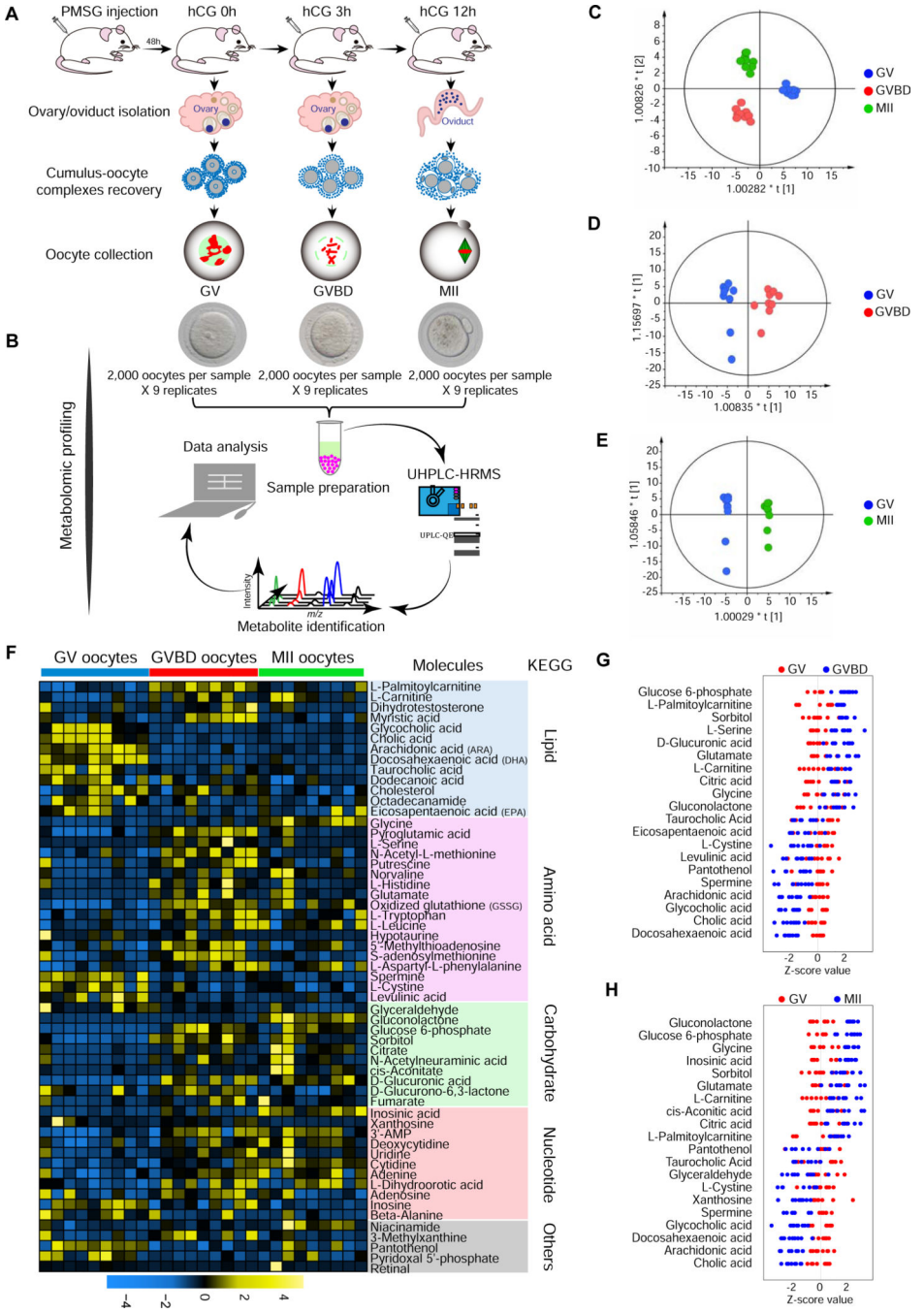

Figure 1. Metabolomic profiling of mouse oocyte maturation.

(A) Illustration of *in vivo* isolation of mouse oocytes at GV, GVBD, and MII stage. (B) Schematic overview of the workflow for metabolome profiling in oocytes. (C-E) OPLS-DA score plot separating GV, GVBD, and MII oocyte samples (Ellipse: Hotelling's T2 99%; C: R2X(cum)=0.607, Q2X(cum)=0.832; D: R2X(cum)=0.52, Q2X(cum)=0.848; E: R2X(cum)=0.584, Q2X(cum)=0.943). (F) Heat map showing the dynamics of 57 differential metabolites during oocyte maturation, classified by metabolic pathways. (G) Z-score plot of 20 representative metabolites from (F) compared between GV and GVBD oocytes (meiotic

resumption). (H) Z-score plot of 20 representative metabolites from (F) compared between GV and MII oocytes (meiotic maturation). Each point represents one metabolite in one sample, colored by stage type. See also Table S1.

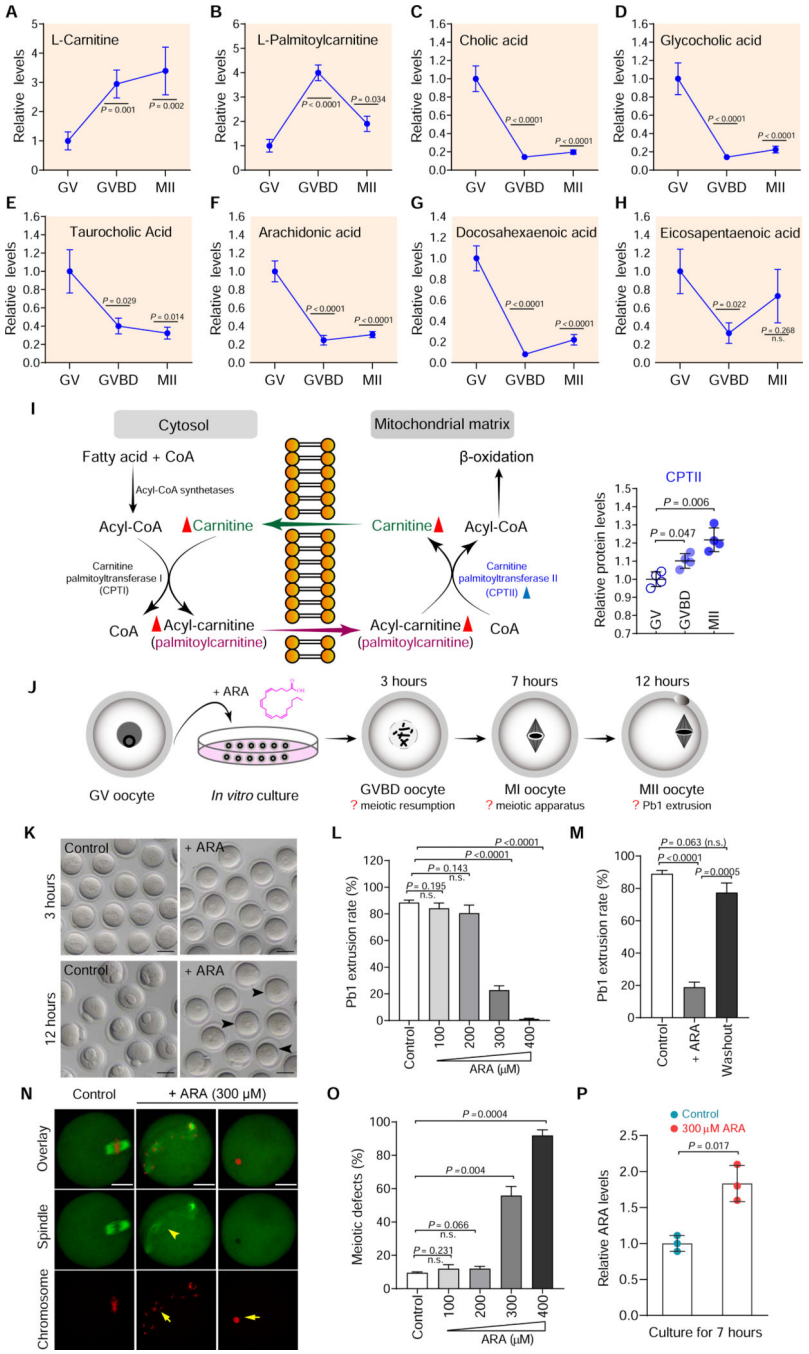

Figure 2. Metabolic features of lipid during oocyte maturation.

(A-H) Relative levels of metabolites related to lipid metabolism in oocytes at different stages. (I) Schematic diagram of carnitine transport system and fatty acid oxidation in the mitochondria. Metabolites increased in maturing oocytes are indicated by red filled triangles, and metabolic enzymes upregulated during maturation are denoted by blue filled triangles. Relative abundance of CPTII protein in oocytes at different stages is shown. (J) Schematic presentation of the experimental protocol to examine the effects of ARA supplementation on oocyte maturation. (K) Bright-field images of control and ARA-treated

oocytes. Arrowheads point to oocytes that fail to extrude a polar body. Scale bars, 50 μm. (L) Quantitative analysis of Pb1 extrusion in control and ARA-treated oocytes. (M) Quantitative analysis of Pb1 extrusion in oocytes after ARA washout. (N) Representative confocal images of control and ARA-treated oocytes stained with α-tubulin antibody to visualize the spindle (green) and with propidium iodide to visualize chromosomes (red). Spindle disorganization and chromosome misalignment are indicated by arrowheads and arrows, respectively. Scale bars, 25 μm. (O) Quantification of control and ARA-treated oocytes with abnormal spindle/chromosomes. (P) Relative ARA levels in control and ARA-treated oocytes. Data are expressed as mean percentage ± SD from three independent experiments in which at least 100 oocytes were analyzed for each group. Student's *t* test was used for statistical analysis in all panels, comparing to GV or control. n.s., not significant. See also Figures S3-S7.

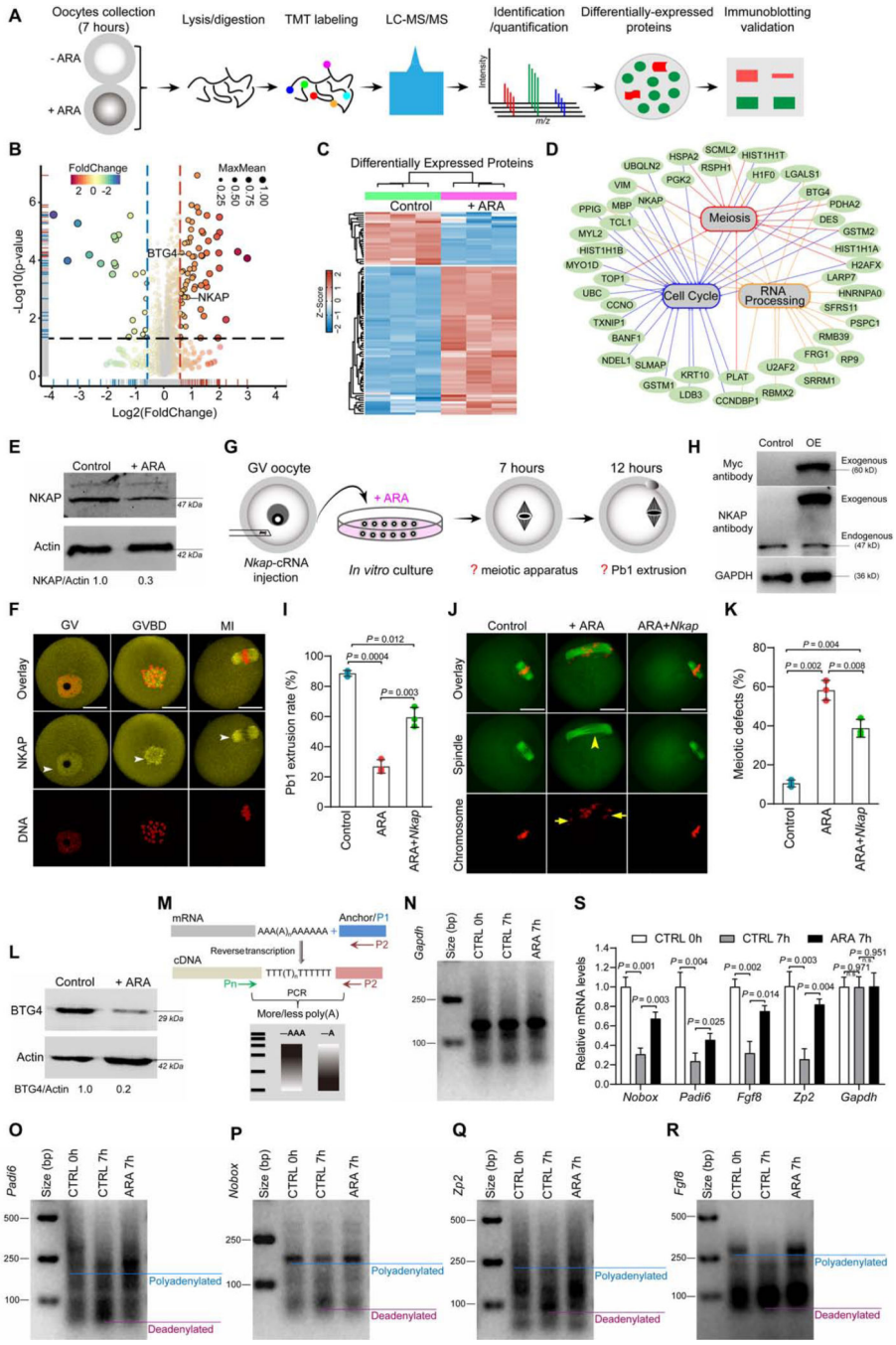

Figure 3. Identification of factors mediating the effects of ARA on oocyte maturation.

(A) Overview of the proteomic workflow for identifying differential protein accumulation. (B) Volcano plot showing the relative abundance of proteins. (C) Heat map of the differentially accumulated proteins between control and ARA-treated oocytes. (D) Gene ontology network enrichment analysis of the proteins with differential accumulation. (E) Western blot analysis of NKAP expression validated the proteomic results (200 oocytes per lane). (F) Cellular distribution of NKAP in oocytes at GV, GVBD and MI stages. Arrowheads point to NKAP signals. Scale bars, 25 μm. (G) Schematic presentation of the

experimental protocol to check whether NKAP overexpression could suppress the defective phenotypes of ARA-treated oocytes. (H) Immunoblotting showing the overexpression (OE) of exogenous NKAP protein in oocytes. (I) Incidence of Pb1 extrusion in indicated oocytes. (J) Representative examples of meiotic spindle and chromosomes in indicated oocytes. Spindle disorganization and chromosome misalignment are indicated by arrowheads and arrows, respectively. Scale bars, 25 μm. (K) Quantitative analysis of meiotic defects in indicated oocytes. At least 100 oocytes for each group were analyzed, and the experiments were conducted three times. (L) Western blot analysis of BTG4 expression validated the proteomic results (200 oocytes per lane). (M) Diagram showing the strategy of the mRNA poly(A) tail (PAT) assay. P1, anchor primer; P2, P1-antisense primer; Pn, gene-specific primer. (N-R) PAT assay showing changes in the poly(A)-tail length for the indicated transcripts in control and ARA-treated oocytes. (S) Relative abundance of the indicated transcripts in control and ARA-treated oocytes, determined by real-time RT-PCR. Error bars, SD. Student's *t* test was used for statistical analysis in all panels. n.s., not significant. See also Figure S8 and Table S3.

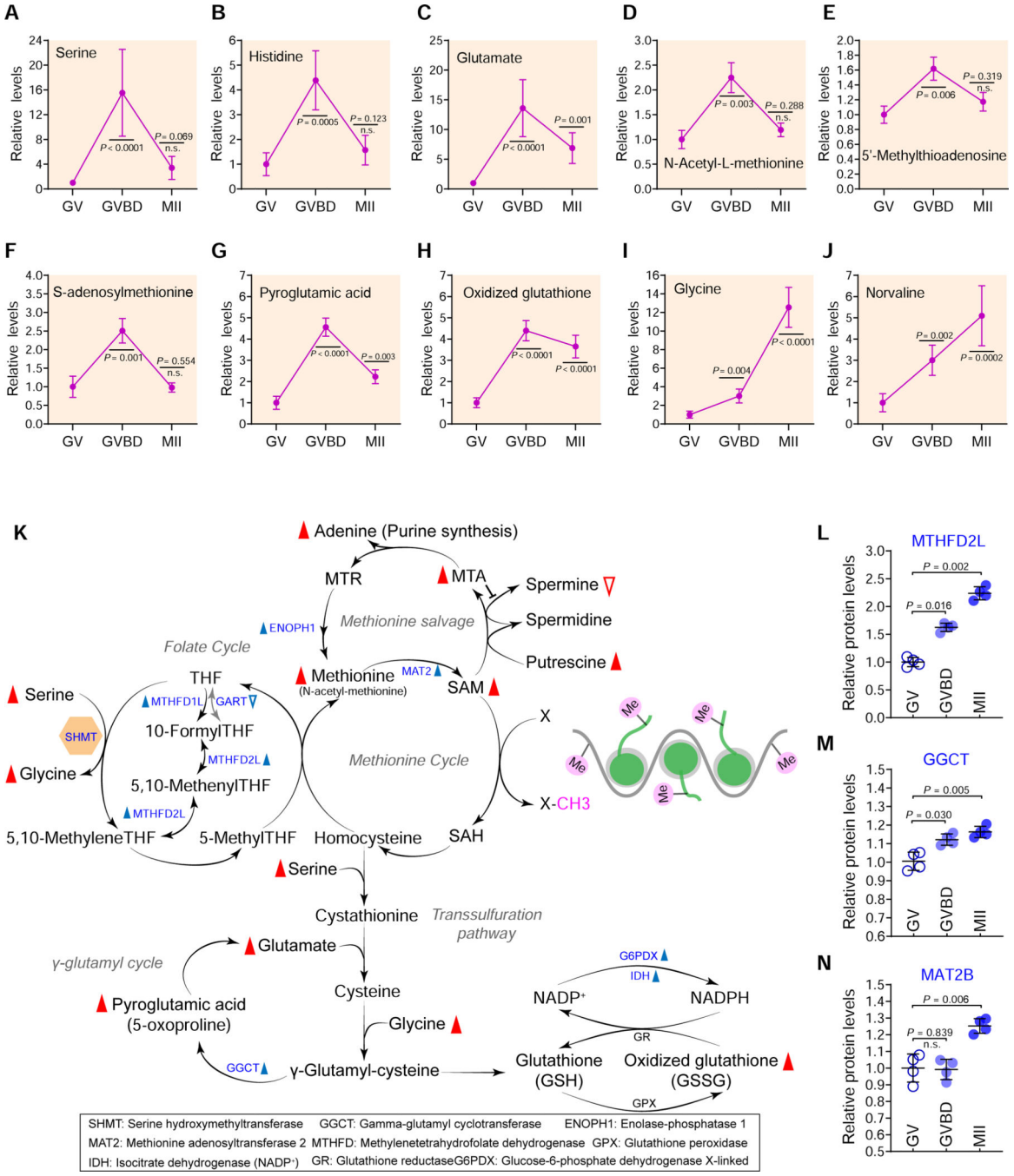

Figure 4. Metabolic changes in amino acids during oocyte maturation.

Relative levels of metabolites related to amino acid metabolism in oocytes at different stages. (K) Schematic diagram of SGOC network during oocyte maturation, derived from metabolomics and proteomics. Metabolites increased and decreased in maturing oocytes are indicated by red filled and empty triangles, respectively. The blue filled and empty triangles denote the metabolic enzymes that were upregulated and downregulated, respectively. (L-N) Relative abundance of the representative enzymes (MTHFD2L, GGCT and MAT2B) involved in the folate/methionine cycle and the transsulfuration pathway. Error bars, SD.

Student's *t* test was used for statistical analysis in all panels, comparing to GV. n.s., not significant. See also Figure S9.

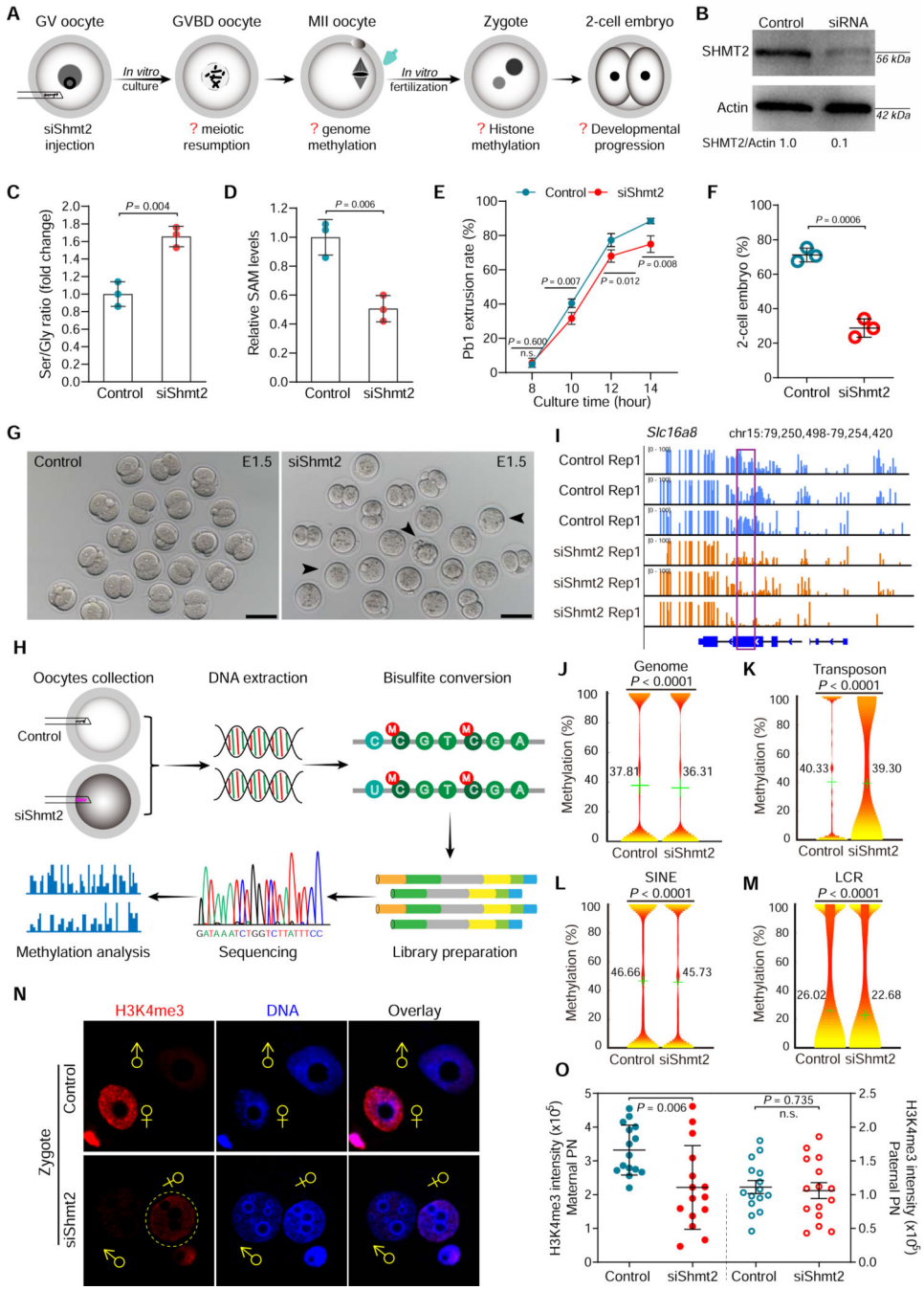

Figure 5. SHMT2 depletion impairs the epigenetic landscape in oocytes.

(A) Schematic presentation of the Shmt2 knockdown experiments. (B) Depletion of endogenous SHMT2 protein was verified by western blot analysis (200 oocytes per lane). (C) Serine-to-Glycine ratio in control (n=300) and siShmt2 (n=300) oocytes. (D) Relative levels of SAM in control (n=300) and siShmt2 (n=300) oocytes. (E) Quantitative analysis of Pb1 extrusion in control (n=102) and siShmt2 (n=105) oocytes. (F) Percentages of control (n=85) and siShmt2 (n=92) oocytes-derived embryos that develop to 2-cell stage during *in vitro* culture. (G) Bright-field images of E1.5 embryos derived from control and siShmt2

oocytes. Scale bars, 100 μm. (H) Flow chart illustrating the BS-Seq procedure for genome-wide methylation analysis. MII oocytes were collected and the DNA was bisulfite converted, followed by library preparation and high-throughput sequencing. (I) Graphical representation of the methylation pattern at *Slc16a8* in control and siShmt2 oocytes. The highlighted region by purple box was chosen to show the significant hypomethylation in this locus following Shmt2 ablation. (J-M) Violin plots showing the methylation levels for distinct genomic features in control and siShmt2 oocytes. Mean methylation levels are indicated by the numerical value and green cross. (N) Images of control and siShmt2 zygotes co-stained with anti-H3K4me3 antibody (red) and Hoechst 33342 (blue). ♂and♀indicate paternal (PN) and maternal (MN) pronucleus, respectively. PB, polar body. (O) Quantification of H3K4me3 fluorescence shown in (N). Each data point represents a zygote (n = 15 for each group). Error bars, SD. Student's *t* test was used for statistical analysis in all panels except for J-M, comparing to control. n.s., not significant. See also Figure S10.

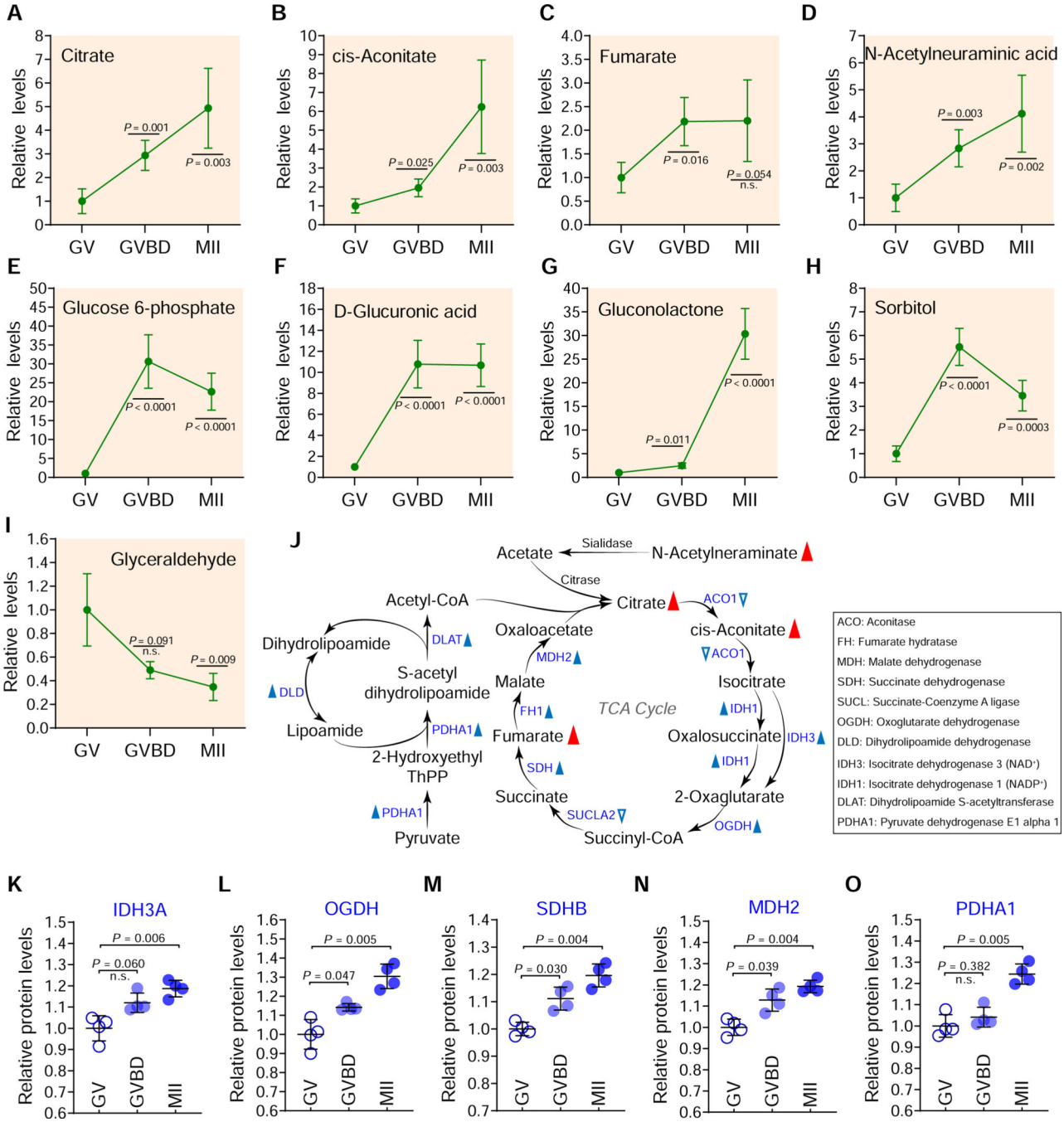

Figure 6. Carbohydrate metabolism during oocyte maturation.

(A-I) Relative levels of metabolites related to carbohydrate metabolism in oocytes at different stages. (J) Schematic diagram of TCA cycle and pyruvate oxidation during oocyte maturation, derived from metabolomics and proteomics. Metabolites increased in maturing oocytes are indicated by red filled triangles. The blue filled and empty triangles denote metabolic enzymes that were upregulated and downregulated, respectively. (K-O) Relative abundance of the representative enzymes (IDH3A, OGDH, SDHB, MDH2, and PDHA1) involved in TCA cycle and pyruvate oxidation. Error bars, SD. Student's *t* test was used for

statistical analysis in all panels, comparing to GV. n.s., not significant. See also Figures S11-S12.

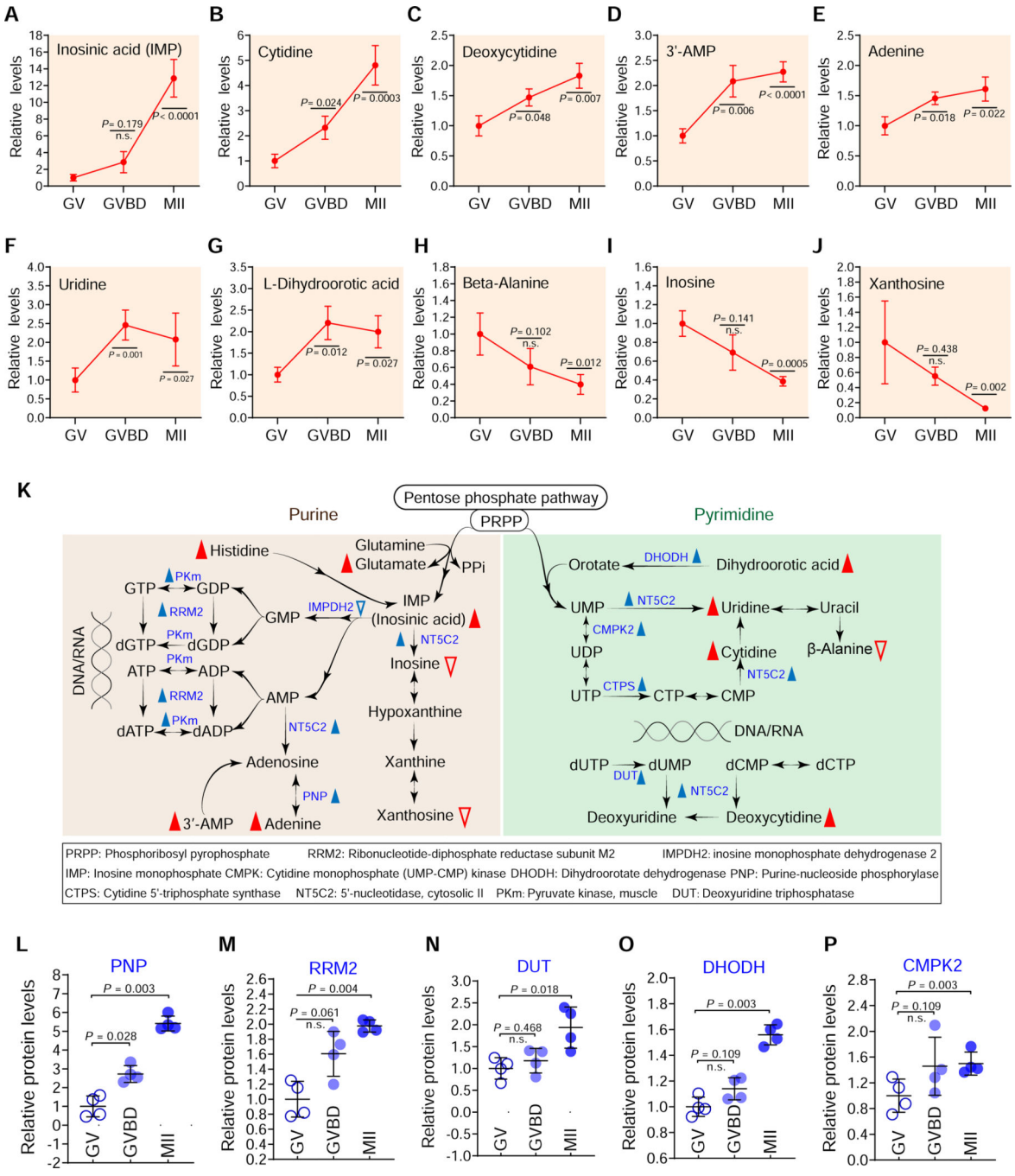

Figure 7. Nucleotide metabolism during oocyte maturation.

Relative levels of metabolites related to nucleotide metabolism in oocytes at different stages. (K) Schematic diagram of purine and pyrimidine metabolism during oocyte maturation, derived from metabolomics and proteomics. Metabolites increased and decreased in maturing oocytes are indicated by red filled and empty triangles, respectively. The blue filled and empty triangles denote metabolic enzymes that were upregulated and downregulated, respectively. (L-P) Relative abundance of the representative enzymes (PNP, PRM2, DUT, DHODH and CMPK2) involved in purine and pyrimidine metabolism. Error bars, SD.

Student's *t* test was used for statistical analysis in all panels, comparing to GV. n.s., not significant. See also Figures S14-S16.

KEY RESOURCES TABLE

REAGENT or RESOURCE	SOURCE	IDENTIFIER
Antibodies		
Rabbit polyclonal anti-SHMT2	Abcam	Cat# ab224428; RRID:AB_2861139
Rabbit monoclonal anti-BTG4	Abcam	Cat# ab206914; RRID:AB_2861140
Sheep polyclonal anti-BubR1	Abcam	Cat# ab28193; RRID:AB_444307
Mouse monoclonal anti-Myc	Abcam	Cat# ab18185; RRID:AB_444307
Rabbit polyclonal anti-H3K4me3	Abcam	Cat# ab8580; RRID:AB_306649
Human anti-Centromere CREST	Fitzgerald Industries International	Cat# 09C-CS1058;
Rabbit polyclonal anti-NKAP	GeneTex	Cat# GTX120929; RRID:AB_2861141
Mouse monoclonal anti-β-actin	Sigma	Cat# A5441; RRID:AB_476744
Mouse monoclonal anti-GAPDH	Proteintech	Cat# HRP-60004; RRID:AB_2737588
Mouse monoclonal anti-α-tubulin-FITC	Sigma	Cat# F2168; RRID:AB_476967
Goat anti-rabbit IgG-FITC	Thermo Fisher	Cat# 65–6111; RRID:AB_2533966
Goat anti-rabbit IgG-HRP	Thermo Fisher	Cat# 81–1620, RRID:AB_2534006
Bacterial and Virus Strains		
TOP10 Competent *E. coli*	TIANGEN	Cat# CB104
Biological Samples		
Oocyte	This Study	N/A
Sperm	This Study	N/A
Embryo	This Study	N/A
Chemicals, Peptides, and Recombinant Proteins		
3'-AMP	Sigma-Aldrich	Cat# A9272
3-Methylxanthine	Adamas	Cat# 13392B
5'-Methylthioadenosine	Sigma-Aldrich	Cat# D5011
Adenine	Aladdin	Cat# A108804
Adenosine	Adamas	Cat# 67712A
Arachidonic acid	Sigma-Aldrich	Cat# A3611
Beta-Alanine	Sigma-Aldrich	Cat# 146064
Cholesterol	Aladdin	Cat# C104029
Cholic acid	Adamas	Cat# 84576A
cis-Aconitic acid	Aladdin	Cat# A111230
Citric acid	Aladdin	Cat# C108872
Cytidine	Adamas	Cat# 74476A
Deoxycytidine	Sigma-Aldrich	Cat# D3897
D-Glucuronic acid	Sigma-Aldrich	Cat# G5269
D-Glucurono-6,3-lactone	Adamas	Cat# 48251A
D-Glutamic acid	Sigma-Aldrich	Cat# V900450
Dihydrotestosterone	Dr.E	Cat# DRE-C10255010

REAGENT or RESOURCE	SOURCE	IDENTIFIER
Docosahexaenoic acid	Sigma-Aldrich	Cat# D2534
Dodecanoic acid	Adamas	Cat# 23651A
Eicosapentaenoic acid	Aladdin	Cat# E100927
Fumaric acid	Adamas	Cat#14061B
Gluconolactone	Adamas	Cat# 89621A
Glucose 6-phosphate	TRC	Cat# G595338
Glyceraldehyde	Sigma-Aldrich	Cat# G5001
Glycine	Adamas	Cat# 65953A
Glycocholic acid hydrate	Sigma-Aldrich	Cat# G2878
Hypotaurine	Sigma-Aldrich	Cat# H1384
Inosine	Adamas	Cat# 67731A
Inosinic acid	Sigma-Aldrich	Cat# I2879
L-Aspartyl-L-phenylalanine	Sigma-Aldrich	Cat# 421669
L-Carnitine	Adamas	Cat# 64024A
L-Cystine	Aladdin	Cat# C108225
L-Dihydroorotic acid	Sigma-Aldrich	Cat# D7128
Levulinic acid	Adamas	Cat# 18284A
L-Histidine	Aladdin	Cat# H108260
L-Leucine	Adamas	Cat# 70880A
L-Palmitoylcarnitine chloride	Sigma-Aldrich	Cat# P4509
L-Serine	Adamas	Cat# 65987B
L-Tryptophan	Adamas	Cat# 79767B
Myristic acid	Adamas	Cat# 64434B
N-Acetyl-L-methionine	Adamas	Cat# 74718A
N-Acetylneuraminic acid	Aladdin	Cat# A100555
Niacinamide	Adamas	Cat# 92273A
Norvaline	Sigma-Aldrich	Cat# N7627
Octadecanamide	Sigma-Aldrich	Cat# O601
Oxidized glutathione	Aladdin	Cat# G105428
Pantothenol	Sigma-Aldrich	Cat# 76200
Putrescine	Aladdin	Cat# D110948
Pyridoxal 5’-phosphate hydrate	Sigma-Aldrich	Cat# P9255
Pyroglutamic acid	Adamas	Cat# 92246A
Retinal	Sigma-Aldrich	Cat# R2500
S-adenosylmethionine	Sigma-Aldrich	Cat# A2408
Sorbitol	Adamas	Cat# 60805A
Spermine	Aladdin	Cat# S109704
Taurocholic Acid sodium salt hydrate	Sigma-Aldrich	Cat# T4009
Uridine	Aladdin	Cat# U108810

REAGENT or RESOURCE	SOURCE	IDENTIFIER
Xanthosine dihydrate	Sigma-Aldrich	Cat# X0750
(−)-Matairesinol	Supelco	Cat# 04157
1-Palmitoyl-Palmitoyl	Sigma-Aldrich	Cat# L5254
2-Furoic acid	Adamas	Cat# 87865A
2-Hydroxypalmitic Acid	Sigma-Aldrich	Cat# H7021
3,4,5-Trimethoxycinnamic acid	Adamas	Cat# 89485A
3-Phenylbutyric Acid	Sigma-Aldrich	Cat# 116807
4-Methylcatechol	Adamas	Cat# 58208B
5-Aminolevulinic acid hydrochloride	Sigma-Aldrich	Cat# A3785
5-Hydroxylysine hydrochloride	Sigma-Aldrich	Cat# H0377
5-Hydroxymethyl-2-Deoxyuridine	Sigma-Aldrich	Cat# H8631
Agmatine Sulfate	Sigma-Aldrich	Cat# A7127
Allantoin	Adamas	Cat# 91922A
Aminocaproic acid	Adamas	Cat# 69197A
Argininosuccinic acid	Sigma-Aldrich	Cat# 73097
Biotin	Adamas	Cat# 67896A
Capric acid	Adamas	Cat# 49153A
Cortisol	Adamas	Cat# 60344A
Cortisone	Aladdin	Cat# C119445
Cyclic AMP	Adamas	Cat# 69704A
Cytosine	Adamas	Cat# 78600A
Dehydroepiandrosterone	Supelco	Cat# D-063
Deoxycholic acid	Adamas	Cat# 85460B
Deoxycholic acid glycine conjugate	Aladdin	Cat# G113438
D-Glucaric acid potassium salt	Sigma-Aldrich	Cat# S4140
Dihydroxyacetone phosphate	Sigma-Aldrich	Cat# 51269
Dodecanedioic acid	Adamas	Cat# 77196A
Estriol	Adamas	Cat# 60385A
Estrone	Adamas	Cat# 63010A
Glycerophosphocholine	Adamas	Cat# 44657A
Glycolic acid	Adamas	Cat# 83663A
Guanine	Aladdin	Cat# G104274
Hexadecanedioic acid	Adamas	Cat# 60631A
Histamine dihydrochloride	Sigma-Aldrich	Cat# 53300
Hyodeoxycholic acid	Aladdin	Cat# H106315
Isocitric acid trisodium salt hydrate	Sigma-Aldrich	Cat# I1252
L-3-Phenyllactic acid	Adamas	Cat# 35411B
L-Cysteine	Adamas	Cat# 62776B
L-Dopa	Adamas	Cat# 68867A

REAGENT or RESOURCE	SOURCE	IDENTIFIER
L-Lysine	Adamas	Cat# 66313B
L-Malic acid	Adamas	Cat# 91942A
L-Phenylalanine	Adamas	Cat# 73340B
Melatonin	Adamas	Cat# 79824B
N-Acetylethylenediamine	Sigma-Aldrich	Cat# 397261
N-Acetylglutamic acid	Adamas	Cat# 16378A
N-Alpha-acetyllysine	Sigma-Aldrich	Cat# A2010
Neopterin	Sigma-Aldrich	Cat# N3386
N-Formyl-L-methionine	Sigma-Aldrich	Cat# F3377
Orotic acid	Adamas	Cat# 74736A
Pentadecanoic acid	Supelco	Cat# 91446
Petroselinic acid	Sigma-Aldrich	Cat# P8750
Prostaglandin E2	Sigma-Aldrich	Cat# P5640
Prostaglandin F2a	TCI	Cat# P1885
Quinic acid	Sigma-Aldrich	Cat# 138622
Rhamnose	Adamas	Cat# 51662A
Riboflavin	Adamas	Cat# 85641A
Succinic acid	Adamas	Cat# 14056B
Syringic acid	Adamas	Cat# 62915A
Taurine	Adamas	Cat# 13304A
Testosterone	Aladdin	Cat# T102169
Tetradecanedioic acid	Sigma-Aldrich	Cat# D221201
Thyroxine	Aladdin	Cat# T106193
Trizma Acetate	Sigma-Aldrich	Cat# V900448
Tryptophanol	Sigma-Aldrich	Cat# 469971
Xanthurenic acid	Sigma-Aldrich	Cat# D120804
M16 medium	Sigma-Aldrich	Cat# M7292
HTF medium	Merck Millipore	Cat# MR-070
KSOM medium	Merck Millipore	Cat# MR-106-D
Milrinone	Sigma-Aldrich	Cat# M4659
Bovine serum albumin	Sigma-Aldrich	Cat# A1470
Mineral oil	Sigma-Aldrich	Cat# M8410
INDO	Selleck Chemicals	Cat# S5010
Sesamin	Selleck Chemicals	Cat# S2392
Curcumin	Selleck Chemicals	Cat# S1848
BWA4C	Sigma-Aldrich	Cat# B7559
propidium iodide	Thermo Fisher	Cat# P3566
Hoechst 33342	Thermo Fisher	Cat# H3570
Anti-fade medium	Vectashield	Cat# H1000

REAGENT or RESOURCE	SOURCE	IDENTIFIER
CM-H2DCFDA	Thermo Fisher	Cat# C6827
Proteinase K	Thermo Fisher	Cat# EO0492
T4 RNA Ligase	Thermo Fisher	Cat# AM2141
AscI endonuclease	New England Biolabs	Cat# R0558S
FseI endonuclease	New England Biolabs	Cat# R0588S
T4 DNA ligase	New England Biolabs	Cat# M0202S
NotI endonuclease	New England Biolabs	Cat# R0189S
DpnI endonuclease	New England Biolabs	Cat# R0176S
Phusion high-fidelity DNA polymerase	New England Biolabs	Cat# M0530L
Critical Commercial Assays		
Arcturus PicoPure RNA Isolation Kit	Thermo Fisher	Cat# KIT0204
Quantitect Reverse Transcription Kit	Qiagen	Cat# 205311
QIAquick PCR Purification Kit	Qiagen	Cat# 28104
SP6 mMESSAGE mMACHINE Kit	Thermo Fisher	Cat# AM1340
Pierce ECL Western Blotting Substrate	Thermo Fisher	Cat# 32106
SuperScript™ III First-Strand Synthesis SuperMix	Thermo Fisher	Cat# 18080–400
TMTsixplex™ Isobaric Label Reagent Set	Thermo Fisher	Cat# 90066
EZ DNA Methylation-Gold Kit	Zymo Research	Cat# D5005
Deposited Data		
Oocytes proteomics data I	This Study	Project accession: PXD018777; username: reviewer55684@ebi.ac.uk; password: mYMGRG0w.
Oocytes proteomics data II	This Study	Project accession: PXD018753; username: reviewer43455@ebi.ac.uk; password: Uz92GHI2.
Oocyte metabolomics data	This Study	See Table S1
Oocyte Bisulfite-seq data.	This Study	GEO: GSE149053
Original/source data	This Study	https://data.mendeley.com/datasets/8tftw77m4z/draft?a=f27e269e-9b60–43f2–9ccb-09c720c7a3bb
Experimental Models: Cell Lines		
N/A	N/A	N/A
Experimental Models: Organisms/Strains		
C57BL/6 mice	Charles River Laboratories	N/A
Oligonucleotides		
siRNA sequences for knockdown experiments	This Study	see Table S4
Primer sequences for overexpression analysis	This Study	see Table S4
Primer sequences for Poly(A) tail assay	This Study	see Table S4
Primer sequences for qRT-PCR	This Study	see Table S4
Recombinant DNA		

REAGENT or RESOURCE	SOURCE	IDENTIFIER
Plasmid: Myc tags in pCS2$^+$	This Study	N/A
Plasmid: Myc tags-Nkap in pCS2$^+$	This Study	N/A
Plasmid: Myc tags-Nkap mutation in pCS2$^+$	This Study	N/A
Plasmid: Myc tags-Shmt2 mutation in pCS2$^+$	This Study	N/A
Plasmid: Myc tags-G6pdx in pCS2$^+$	This Study	N/A
Software and Algorithms		
ImageJ	NIH	https://imagej.nih.gov/ij/
Prism (V7.0)	GraphPad	https://www.graphpad.com/scientific-software/prism/
R (V2.15.0)	(Davey et al., 1997)	http://cran.r-project.org/
ZEN	ZEISS	https://www.zeiss.com/microscopy/int/downloads.html
TraceFinder (V3.1)	Thermo Fisher	https://www.thermofisher.com/us/en/home/industrial/mass-spectrometry/liquid-chromatography-mass-spectrometry-lc-ms/lc-ms-software/lc-ms-data-acquisition-software/tracefinder-software.html
SIMCA-P (V14.0)	Umetrics	https://umetrics.com/products/simca
KEGG Mapper (V4.1)	Kanehisa et al., 2020	https://www.genome.jp/kegg/mapper.html
MaxQuant (V1.2.2.5)	Cox and Mann, 2008	https://maxquant.net/maxquant/
DAVID	Huang et al., 2009	https://david.ncifcrssf.gov/
Perseus software platform (V1.6.2.3)	Tyanova et al., 2016	https://maxquant.net/perseus/
Pathway Studio (V 6.00)	Nikitin et al., 2003	https://www.pathwaystudio.com/
Cytoscape (V3.7.2)	Shannon et al., 2003	https://cytoscape.org/
Trim galore	https://github.com/FelixKrueger/TrimGalore	https://www.bioinformatics.babraham.ac.uk/projects/trim_galore/
Bismark	Krueger et al., 2011	https://www.bioinformatics.babraham.ac.uk/projects/bismark/
Metilene	Jühling et al., 2015	https://www.bioinf.uni-leipzig.de/Software/metilene/
IGV	Robinson et al., 2011	https://igv.org/
UCSC Genome Browser	University of California Santa Cruz	http://genome.ucsc.edu/
BEDOPS	Neph et al., 2012	https://bedops.readthedocs.io/en/latest/index.html
Other		
N/A	N/A	N/A